1   **Reprogramming of the FOXA1 cistrome in treatment-emergent neuroendocrine prostate**
2   **cancer**
3
4   **Authors**

5   Sylvan C. Baca[1-3], David Y. Takeda[4], Ji-Heui Seo[1,2], Justin Hwang[1], Sheng Yu Ku[1], Rand
6   Arafeh[1], Taylor Arnoff[1] , Supreet Agarwal[4], Connor Bell[1,2], Edward O'Connor[1,2], Xintao Qiu[1,2],
7   Sarah Abou Alaiwi[1,2], Rosario I. Corona[5,6], Marcos A. S. Fonseca[5], Claudia Giambartolomei[7,8],
8   Paloma Cejas[1,2], Klothilda Lim[1,2], Monica He[1,2], Anjali Sheahan[9], Amin Nassar[1], Jacob E.
9   Berchuck[1,2], Lisha Brown[10], Holly M. Nguyen[10], Ilsa M. Coleman[11], Arja Kaipainen[11], Navonil De
10   Sarkar[11], Peter S. Nelson[11], Colm Morrissey[10], Keegan Korthauer[12,13], Mark M. Pomerantz[1,2],
11   Leigh Ellis[9,14], Bogdan Pasaniuc[7], Kate Lawrenson[5,6], Kathleen Kelly[4], Amina Zoubeidi[15,16],
12   William C. Hahn[1,3], Himisha Beltran[1], Henry W. Long[1,2], Myles Brown[1,2], Eva Corey[10], Matthew
13   L. Freedman[1-3] *
14

15   **Affiliations:**
16   [1] Department of Medical Oncology, Dana-Farber Cancer Institute, Boston, MA, USA
17   [2] Center for Functional Cancer Epigenetics, Dana-Farber Cancer Institute, Boston, MA, USA
18   [3] The Eli and Edythe L. Broad Institute, Cambridge, MA, USA
19   [4] Laboratory of Genitourinary Cancer Pathogenesis, Center for Cancer Research, National
20   Cancer Institute, NIH, Bethesda, Maryland
21   [5] Department of Obstetrics and Gynecology and the Women's Cancer Program at the Samuel
22   Oschin Comprehensive Cancer Institute, Cedars-Sinai Medical Center, Los Angeles, CA, USA
23   [6] Center for Bioinformatics and Functional Genomics, Department of Biomedical Sciences,
24   Cedars-Sinai Medical Center, Los Angeles, CA, USA
25   [7] Department of Pathology and Laboratory Medicine, David Geffen School of Medicine,
26   University of California Los Angeles, Los Angeles, CA, USA
27   [8] Istituto Italiano di Tecnologia, Genova, Italy
28   [9] Department of Oncologic Pathology, Dana-Farber Cancer Institute, Boston, MA, USA
29   [10] Department of Urology, University of Washington, Seattle, WA, USA
30   [11] Divisions of Human Biology and Clinical Research, Fred Hutchinson Cancer Research
31   Center, Seattle, WA, USA
32   [12] Department of Data Sciences, Dana-Farber Cancer Institute, Boston, MA, USA
33   [13] Department of Biostatistics, Harvard T.H. Chan School of Public Health, Boston, MA, USA

34   [14] Department of Pathology, Brigham & Women's Hospital and Harvard Medical School, Boston,

35   MA, USA

36   [15] Vancouver Prostate Centre, Vancouver, British Columbia, Canada

37   [16] Department of Urologic Sciences, Faculty of Medicine, University of British Columbia, British

38   Columbia, Canada

39

40   * Corresponding author

41

42   **Abstract:**

43   Lineage plasticity, the ability of a cell to alter its identity, is an increasingly common

44   mechanism of adaptive resistance to targeted therapy in cancer[1,2]. An archetypal example is the

45   development of neuroendocrine prostate cancer (NEPC) after treatment of prostate

46   adenocarcinoma (PRAD) with inhibitors of androgen signaling. NEPC is an aggressive variant of

47   prostate cancer that aberrantly expresses genes characteristic of neuroendocrine (NE) tissues

48   and no longer depends on androgens. To investigate the epigenomic basis of this resistance

49   mechanism, we profiled histone modifications in NEPC and PRAD patient-derived xenografts

50   (PDXs) using chromatin immunoprecipitation and sequencing (ChIP-seq). We identified a vast

51   network of *cis*-regulatory elements (N~15,000) that are recurrently activated in NEPC. The

52   FOXA1 transcription factor (TF), which pioneers androgen receptor (AR) chromatin binding in

53   the prostate epithelium[3,4], is reprogrammed to NE-specific regulatory elements in NEPC.

54   Despite loss of dependence upon AR, NEPC maintains FOXA1 expression and requires FOXA1

55   for proliferation and expression of NE lineage-defining genes. Ectopic expression of the NE

56   lineage TFs ASCL1 and NKX2-1 in PRAD cells reprograms FOXA1 to bind to NE regulatory

57   elements and induces enhancer activity as evidenced by histone modifications at these sites.

58   Our data establish the importance of FOXA1 in NEPC and provide a principled approach to

59   identifying novel cancer dependencies through epigenomic profiling.

60

61   **Introduction:**

62   In recent years, potent AR pathway inhibitors have extended the survival of patients with

63   metastatic prostate cancer[5,6]. Prostate tumors inevitably escape AR inhibition through

64   reactivation of AR signaling or, increasingly, via lineage plasticity[1,7]. The mechanisms underlying

65   lineage plasticity remain unclear but likely involve transdifferentiation of PRAD to NEPC rather

66   than *de novo* emergence of NEPC. NEPC and PRAD tumors from an individual patient share

67   many somatic DNA alterations, implying a common ancestral tumor clone[8]. While the genomic

68   profiles of NEPC and PRAD are relatively similar, their gene expression profiles and clinical

69   behavior differ markedly[9]. We therefore set out to characterize epigenomic differences between

70   NEPC and PRAD, hypothesizing that reprogramming of distinct regulatory elements drives their

71   divergent phenotypes.

72

73   **Results:**

74   We performed ChIP-seq for the histone post-translational modification H3K27ac to

75   identify active regulatory elements in the LuCaP PDX series[10], a set of xenografts derived from

76   advanced PRAD (N=22) and treatment-emergent NEPC (N=5). We identified a median of

77   55,095 H3K27ac peaks per sample (range 37,599-74,640) (Supplementary Table 1). Notably,

78   the transcriptomes of the LuCaP PDXs reflect differences in gene expression observed between

79   clinical PRAD and NEPC metastases (Supplementary Fig. 1a), indicating their relevance to

80   clinical prostate cancer.

81   Unsupervised hierarchical clustering and principal component analysis based on

82   genome-wide H3K27 acetylation cleanly partitioned NEPC and PRAD LuCaP PDXs (Fig. 1a,

83   Supplementary Fig. 1b, c). We identified 14,985 sites with eight-fold or greater increases in

84   H3K27 acetylation in NEPC compared to PRAD at an adjusted p-value of 10^{-3}. We termed these

85   sites neuroendocrine-enriched candidate regulatory elements ("Ne-CREs"; Fig. 1b,

86   Supplementary Table 2, Supplementary Fig. 1d). A smaller set of sites (4,338) bore greater

87   H3K27ac signal in PRAD (termed "Ad-CREs"). Liver metastases from clinical NEPC and PRAD

88   demonstrated enrichment of H3K27ac at Ne-CREs and Ad-CREs, respectively, confirming that

89   the LuCaP PDX models reflect lineage-specific epigenomic features of clinical prostate tumors

90   (Supplementary Fig. 1e).

91   Ad-CREs were found near prostate lineage genes such as *KLK3*, *HOXB13,* and *NKX3-*

92   *1*, while Ne-CREs resided near genes enriched for neuronal and developmental annotations,

93   including *CHGA*, *ASCL1*, and *SOX2*[11] (Fig. 1c, Supplementary Table 3). Genes with higher

94   expression in NEPC compared to PRAD were enriched for nearby Ne-CREs (Supplementary

95   Fig. 1f) and formed three-dimensional contacts with a greater number of Ne-CREs as assessed

96   by H3K27ac HiChIP (Fig. 1d, Supplementary Fig. 1g-h, and Supplementary Tables 4 and 5).

97   For example, *ASCL1,* which encodes a neural lineage TF that is highly upregulated in NEPC

98   (Supplementary Fig. 1a), interacts with 15 gene-distal Ne-CREs between 280kb and 465kb

99   telomeric to *ASCL1*, including two novel NEPC-restricted super-enhancers within intronic

100   regions of *C12ORF42* (Fig. 1e). These results suggest that Ne-CREs regulate neuroendocrine

101   transcriptional programs through interaction with NEPC gene promoters.

102   We nominated candidate TFs that may orchestrate NEPC lineage gene expression by
103   binding to Ne-CREs. Lineage-defining TF genes often reside within densely H3K27-acetylated
104   super-enhancers[12] and form core regulatory circuits, or "cliques", by mutual binding of one
105   another's *cis*-regulatory regions[13,14]. Several TFs showed clique enrichment specifically in
106   NEPC (Fig. 1f) and/or were encompassed by NEPC-restricted super-enhancers (Supplementary
107   Fig. 2), including known NE lineage TFs (*e.g.*, *ASCL1* and *INSM1*) and novel candidates such
108   as *HOXB2-5*.

109   Notably, a single TF gene, *FOXA1*, demonstrated clique enrichment in all NEPC and
110   PRAD LuCaP PDXs (Fig. 1f). FOXA1 is a pioneer TF of endodermal tissues[3] with a critical role
111   in prostate development[4] but no characterized function in NEPC. The forkhead motif recognized
112   by FOXA1 was the second most significantly enriched nucleotide sequence within Ne-CREs
113   (Fig. 1g). FOXA2, a previously-reported NEPC TF[15], does not wholly account for the forkhead
114   motif enrichment because FOXA2 was not expressed in several NEPC samples (Figs. 2a,b;
115   Supplementary Fig. 3a). In contrast, FOXA1 was expressed in all NEPCs (Fig 2a-b; Table S6)
116   as well as in resident neuroendocrine cells of benign prostate tissue (Supplementary Fig. 3).

117   Multiple lines of investigation supported a pivotal role of FOXA1 in NEPC. A super-
118   enhancer encompassed *FOXA1* in all NEPC LuCaP PDXs (Fig. 2c, Supplementary Fig. 2). In
119   NEPC, the *FOXA1* promoter shed contacts with its regulatory region identified in PRAD[16] and
120   looped to a distinct NEPC-restricted super-enhancer (Fig. 2d). Both the distal superenhancer
121   and promoter were co-bound by FOXA1 and ASCL1, suggesting an auto-regulatory circuit that
122   is characteristic of master transcriptional regulators[17]. Suppression of FOXA1 in a variety of
123   NEPC cellular models[18,19] demonstrated that FOXA1 is essential for cellular proliferation (Fig.
124   2e-g) and expression of NE markers, including NE lineage TFs such as FOXA2 and INSM1
125   (Fig. 2h). Analysis of a published shRNA screen confirmed a dependency on FOXA1 in the
126   NEPC cell line NCI-H660 (Fig. 2i). Thus, FOXA1 exhibits several features of a master
127   transcriptional regulator in NEPC.

128   We profiled FOXA1 binding sites in NEPC and PRAD using ChIP-seq. FOXA1 relocates
129   to a distinct set of binding sites in NEPC PDXs (Fig. 3a), which overlap with the majority of Ne-
130   CREs (Fig. 3b). In PRAD, Ne-CREs were devoid of FOXA1 binding and heterochromatic as
131   assayed by ATAC-seq, but they acquired FOXA1 binding and chromatin accessibility in NEPC
132   (Fig. 3c). Conversely, Ad-CREs lost FOXA1 binding in NEPC and became less accessible by
133   ATAC-seq. To contextualize the extent of FOXA1 reprogramming in NEPC, we compared
134   FOXA1 binding profiles in normal prostate epithelium, localized PRAD, and PDXs derived from
135   metastatic PRAD. At the same level of stringency, fewer than 500 sites exhibited differential

4

136   FOXA1 binding between these categories; by comparison, FOXA1 binding was gained at

137   20,935 and lost at 29,308 sites in NEPC compared to metastatic PRAD (Fig. 3d).

138   We sought to understand the mechanism by which FOXA1 binding is reprogrammed in

139   NEPC. In addition to DNA sequence, cooperative binding with partner TFs is an important

140   determinant of pioneer factor localization[20]. Since the motifs recognized by ASCL1 and NKX2-1

141   were highly enriched at Ne-CREs (Fig. 1g), we tested whether overexpression of these TFs in

142   the PRAD cell line LNCaP could induce FOXA1 binding at Ne-CREs. Overexpression of ASCL1

143   and NKX2-1 (A+N) increased FOXA1 binding at NEPC-enriched FOXA1 binding sites (Fig.

144   4a,b) and induced H3K27 acetylation of Ne-CREs (Fig. 4c-f). ASCL1 co-localized with FOXA1

145   at NEPC-enriched FOXA1 binding sites and Ne-CREs (Fig. 4g-h). A+N expression recapitulated

146   global transcriptional changes between NEPC and PRAD, including suppression of *AR* and

147   induction of *SYP* and *CHGA* (Fig. 4i-k). Thus, ectopic expression of ASCL1 and NKX2-1 is

148   sufficient to partially reprogram FOXA1 binding in PRAD to Ne-CREs and induce *de novo*

149   H3K27 acetylation at these regions, with resultant NEPC gene expression.

150   Despite intense interest, it remains unclear why PRAD can adopt a seemingly unrelated

151   lineage to overcome androgen blockade, while most cancers do not dramatically alter their

152   cellular identity throughout treatment. Lineage tracing studies have demonstrated that the

153   epithelial cells that give rise to PRAD share a common developmental progenitor with resident

154   neuroendocrine cells in the prostate[21,22]. In this common progenitor cell, Ne-CREs and their

155   FOXA1 binding sites might be physiologically poised for activation upon commitment to a

156   neuroendocrine lineage. In support of this model, genes that are highly expressed in normal

157   neuroendocrine prostate cells are also highly expressed in NEPC (Fig. 5a), and are enriched for

158   nearby Ne-CREs and NEPC-restricted FOXA1 binding sites (Fig. 5b). Additionally, Ne-CREs

159   are relatively hypomethylated in normal prostate tissue and PRAD despite absence of H3K27

160   acetylation, a feature of decommissioned enhancers that were active in development (Fig.

161   5c)[23,24].

162   We hypothesized that a neuroendocrine epigenomic program is encoded in the

163   developmental history of the prostate, thereby priming NEPC genes for inappropriate activation

164   under the selective pressure of androgen blockade. Consistent with this hypothesis, many

165   genes that become highly expressed in NEPC have "bivalent" (H3K4me3[+]/H3K27me3[+])

166   promoter histone marks in normal prostate tissue and PRAD (Fig. 6a). Bivalent genes are

167   thought to be poised for lineage-specific activation upon removal of H3K27me3 at the

168   appropriate stage of development[25-27]. Our data suggested that a similar principle underlies

169   transcriptional changes in prostate cancer lineage plasticity. H3K27me3 levels decreased in

170 NEPC compared to PRAD at 633 gene promoters, which were enriched for binding sites of the

171 REST repressor of neuronal lineage transcription[28] (Supplementary Fig. 4). Similar numbers of

172 these promoters were bivalent (H3K4me3$^+$/H3K27me3$^+$; n=195) and repressed (H3K4me3$^-$

173 /H3K27me3$^+$; n=229) in PRAD (Fig. 6b). Critically, however, genes with bivalent (H3K4me3$^+$)

174 promoters in PRAD became more highly expressed in NEPC (Fig. 6c) than H3K4me3$^-$ genes.

175 These bivalent genes, which included NEPC TFs *ASCL1, INSM1,* and *SOX2*, may have been

176 prepared for activation in the development of a prostate progenitor cell. Their residual H3K4me3

177 and promoter hypomethylation (Fig. 6d) suggest heightened potential for re-activation[24] in

178 NEPC with the disruption of pro-luminal AR-driven transcriptional programs.

179

180 **Discussion:**

181 In summary, our work demonstrates that the *cis*-regulatory landscape of prostate cancer

182 is extensively reprogrammed in NEPC. Epigenomic profiling of human tumors identified a critical

183 role of FOXA1 in this process, which perhaps has been overlooked because candidate drivers

184 of NEPC have been nominated and prioritized mainly based on differential expression or

185 somatic DNA alterations[9,11,29,30]. FOXA1 has been reported to *inhibit* neuroendocrine

186 differentiation of prostate adenocarcinoma, based on the observations that FOXA1 is

187 downregulated in NEPC and that FOXA1 knock-down induces neuroendocrine features in

188 PRAD cell lines[31]. Our data demonstrate that FOXA1 remains crucial in NEPC despite

189 consistent, modest transcript downregulation in NEPC compared to PRAD. Our H3K27ac

190 HiChIP data reveal that in NEPC, *FOXA1* contacts distal super-enhancers that are distinct from

191 its PRAD enhancers and contain binding sites for NE-associated TFs such as ASCL1 and

192 INSM1 (Fig 2d. and Supplementary Fig. 5). Thus, an NEPC-specific regulatory program may

193 maintain FOXA1 expression at lower levels that are conducive to NE gene expression,

194 reconciling our findings with the reported pro-neuroendocrine effects of partial FOXA1

195 suppression in PRAD[31]. While our data show that FOXA1 is essential in NEPC, further studies

196 are required to determine if FOXA1 cistrome reprogramming directly activates Ne-CREs and to

197 assess its role dynamic lineage plasticity.

198 FOXA1 may have a more general role in controlling neuroendocrine differentiation. For

199 example, in small cell lung cancer (SCLC), a neuroendocrine lung cancer variant that can

200 emerge *de novo* or from *EGFR*-mutant lung adenocarcinoma after targeted kinase inhibition,

201 *FOXA1* is highly expressed and encompassed by a super-enhancer[32]. We observe extensive

202 H3K27 acetylation in SCLC cell lines specifically at Ne-CREs and NEPC-enriched FOXA1

203 binding sites, suggesting similar enhancer usage between in SCLC and NEPC (Supplementary

6

204 Fig. 6), consistent with recent reports[29,33]. Ultimately, therapeutic targeting of FOXA1 and/or

205 proteins that collaborate with or covalently modify this TF presents an attractive strategy to

206 inhibit lineage plasticity, as FOXA1 is a common vulnerability in both PRAD and NEPC.

207

208 **Methods:**

209 **Patient-derived xenograft and tissue specimens**

210 LuCaP patient-derived xenografts (PDXs) have been described previously[10,34-37] with the

211 exception of LuCaP 208.1. LuCaP 208.1 was derived from treatment-emergent NEPC and

212 demonstrates typical small cell histology. All LuCaP PDXs were derived from resected

213 metastatic prostate cancer with informed consent of patient donors as described previously[10]

214 under a protocol approved by the University of Washington Human Subjects Division IRB. Liver

215 metastasis needle biopsy specimens were obtained from the Dana-Farber Cancer Institute Gelb

216 Center biobank and were collected under DFCI/Harvard Cancer Center IRB-approved protocols.

217 Metastases were reviewed by a clinical pathologist. The NEPC metastasis was obtained from a

218 patient with *de novo* metastatic prostate adenocarcinoma after 17 months of androgen

219 deprivation therapy with leuprolide and bicalutamide. Immunohistochemistry revealed staining

220 for synaptophysin, chromogranin, and NKX3-1 (weak), and absence of RB1, AR, and PSA.

221

222 **Epigenomic profiling**

223 *Histone mark ChIP in LuCaP PDXs*

224 Chromatin immunoprecipitation (ChIP) for histone marks (H3K27ac, H3K27me3, and

225 H3K4me3) in PDXs was performed as previously described[38]. Briefly, 20-30 mg of frozen tissue

226 was pulverized using the CryoPREP dry impactor system (Covaris). The tissue was then fixed

227 using 1% formaldehyde (Thermo fisher) in PBS for 18 minutes at 37 degrees Celsius and was

228 quenched with 125 mM glycine. Chromatin was lysed in ice-cold lysis buffer (50mM Tris, 10mM

229 EDTA, 1% SDS with protease inhibitor) and was sheared to 300~800 bp using the Covaris

230 E220 sonicator (105 watt peak incident power, 5% duty cycle, 200 cycles/burst) for 10 min. Five

231 volumes of dilution buffer (1% Triton X-100, 2 mM EDTA, 150 mM NaCl, 20 mM Tris HCl pH

232 8.1) were added to chromatin. The sample was then incubated with antibodies (H3K27ac,

233 Diagenode, C15410196; H3K27me3, Cell Signaling 9733S; H3K4me3, Diagenode C15410003

234 premium) coupled with protein A and protein G beads (Life Technologies) at 4 degrees Celsius

235 overnight. The chromatin was washed with RIPA wash buffer (100 mM Tris pH 7.5, 500 mM

236 LiCl, 1% NP-40, 1% sodium deoxycholate) for 10 minutes six times and rinsed with TE buffer

237 (pH 8.0) once.

7

238

239 *Transcription factor ChIP in PDXs.*

240 ChIP for transcription factors (FOXA1 and ASCL1) in PDXs was performed as

241 previously described[38]. Briefly, 50-80 mg of frozen tissue was pulverized using the CryoPREP

242 dry impactor system (Covaris). The tissue was then fixed using 1% formaldehyde (Thermo

243 fisher) in PBS for 18 minutes at room temperature and was quenched with 125 mM glycine.

244 Chromatin was lysed in 1mL ice-cold Myer's Lysis buffer (0.1% SDS, 0.5% sodium

245 deoxycholate and 1% NP-40 with protease inhibitor) and was sheared to 300~800 bp using the

246 Covaris E220 sonicator (140 PIP, 5% duty cycle, 200 cycles/burst) for 20 min. The sample was

247 then incubated with antibodies (FOXA1, ab23738, Abcam; ASCL1, ab74065) coupled with

248 protein A and protein G beads (Life Technologies) at 4 degrees Celsius overnight. The

249 chromatin was washed with RIPA wash buffer (100 mM Tris pH 7.5, 500 mM LiCl, 1% NP-40,

250 1% sodium deoxycholate) for 10 minutes six times and rinsed with TE buffer (pH 8.0) once.

251

252 *LNCaP ChIP*

253 ChIP in LNCaP was performed as previously described[38]. 10 million cells were fixed

254 with 1% formaldehyde at room temperature for 10 minutes and quenched. Cells were collected

255 in lysis buffer (1% NP-40, 0.5% sodium deoxycholate, 0.1% SDS and protease inhibitor

256 (#11873580001, Roche) in PBS)[39]. Chromatin was sonicated to 300-800 bp using a Covaris

257 E220 sonicator (140 watt peak incident power, 5% duty cycle, 200 cycleburtst). Antibodies

258 (FOXA1, ab23738, Abcam; H3K27ac, C15410196, Diagenode; ASCL1, ab74065) were

259 incubated with 40 µl of Dynabeads protein A/G (Invitrogen) for at least 6 hours before

260 immunoprecipitation of the sonicated chromatin overnight. Chromatin was washed with LiCl

261 wash buffer (100 mM Tris pH 7.5, 500 mM LiCl, 1% NP-40, 1% sodium deoxycholate) 6 times

262 for 10 minutes sequentially.

263

264 *ChIP sequencing*

265 Sequencing libraries were generated from purified IP sample DNA using the

266 ThruPLEX-FD Prep Kit (Rubicon Genomics). Libraries were sequenced using 150-base paired

267 end reads on an Illumina platform (Novogene).

268

269 *ATAC-seq*

270 LuCaP PDX tissues were resuspended and dounced in 300 ul of RSB buffer (10 mM

271 Tris-HCl pH 7.4, 10 mM NaCl, and 3 mM MgCl2 in water) containing 0.1% NP40, 0.1% Tween-

272 20, and 0.01% digitonin. Homogenates were transferred to a 1.5 ml microfuge tube and

273 incubated on ice for 10 minutes. Nuclei were filtered through a 40 μm cell strainer and nuclei

274 were washed with RSB buffer and counted. 50,000 nuclei were resuspended in 50 μl of

275 transposition mix[40] (2.5 μl transposase (100 nM final), 16.5 μl PBS, 0.5 μl 1% digitonin, 0.5 μl

276 10% Tween-20, and 5 μl water) by pipetting up and down six times. Transposition reactions

277 were incubated at 37 C for 30 minutes in a thermomixer with shaking at 1,000 r.p.m. Reactions

278 were cleaned with Qiagen columns. Libraries were amplified as described previously[41] and

279 sequenced on an Illumina Nextseq 500 with 35 base paired-end reads.

280

281 **ChIP-seq data analysis**

282 ChIP-sequencing reads were aligned to the human genome build hg19 using the

283 Burrows-Wheeler Aligner (BWA) version 0.7.15[42]. Non-uniquely mapping and redundant reads

284 were discarded. MACS v2.1.1.20140616[43] was used for ChIP-seq peak calling with a q-value

285 (FDR) threshold of 0.01. ChIP-seq data quality was evaluated by a variety of measures,

286 including total peak number, FrIP (fraction of reads in peak) score, number of high-confidence

287 peaks (enriched > ten-fold over background), and percent of peak overlap with DHS peaks

288 derived form the ENCODE project. ChIP-seq peaks were assessed for overlap with gene

289 features and CpG islands using annotatr[44]. IGV[45] was used to visualize normalized ChIP-seq

290 read counts at specific genomic loci. ChIP-seq heatmaps were generated with deepTools[46] and

291 show normalized read counts at the peak center ± 2kb unless otherwise noted. Overlap of ChIP-

292 seq peaks was assessed using BEDTools. Peaks were considered overlapping if they shared

293 one or more base-pairs.

294

295 *Identification and annotation of PRAD- and NEPC-enriched ChIP-seq peaks*

296 Sample-sample clustering, principal component analysis, and identification of lineage-

297 enriched peaks were performed using Mapmaker (https://bitbucket.org/cfce/mapmaker), a ChIP-

298 seq analysis pipeline implemented with Snakemake[47]. ChIP-seq data from PRAD and NEPC

299 LuCaP PDXs were compared to identify H3K27ac, H3K27me3, and FOXA1 peaks with

300 significant enrichment in the NEPC or PRAD lineage. Only LuCaP PDXs from distinct patients

301 were included, with the exception of the H3K27me3 differential peak analysis, which included

302 both LuCaP 145.1 and 145.2, two LuCaP PDXs derived from distinct NEPC metastases from a

303 single patient. A union set of peaks for each histone modification or TF was created using

304 BEDTools. narrowPeak calls from MACS were used for H3K27ac and FOXA1, while broadPeak

305 calls were used for H3K27me3. The number of unique aligned reads overlapping each peak in

9

306   each sample was calculated from BAM files using BEDtools. Read counts for each peak were

307   normalized to the total number of mapped reads for each sample. Quantile normalization was

308   applied to this matrix of normalized read counts. Using DEseq2[48], lineage-enriched peaks were

309   identified at the indicated FDR-adjusted p-value (padj) and $\log_2$ fold-change cutoffs (H3K27ac,

310   padj < 0.001, $|\log_2$ fold-change$|$ > 3; FOXA1, padj < 0.001, $|\log_2$ fold-change$|$ > 2; H3K27me3,

311   padj < 0.01, $|\log_2$ fold-change$|$ > 1). Unsupervised hierarchical clustering was performed based

312   on Spearman correlation between samples. Principal component analysis was performed using

313   the prcomp R function. Enriched *de novo* motifs in differential peaks were detected using

314   HOMER version 4.7. The top non-redundant motifs were ranked by adjusted p-value.

315   The GREAT tool[49] was used to asses for enrichment of Gene Ontology (GO) and

316   MSigDB perturbation annotations among genes near differential ChIP-seq peaks, assigning

317   each peak to the nearest gene within 500kb. The cistromedb toolkit

318   (http://dbtoolkit.cistrome.org/) was used to compare ChIP-seq peaks for overlap with peaks from

319   a large database of uniformly analyzed published ChIP-seq data (quantified as a "GIGGLE

320   score")[50]. Published TFs and histone marks were ranked by similarity to the querry dataset

321   based on the top 1,000 peaks in each published dataset. Prior to cistromedb toolkit analysis,

322   ChIPseq peaks were mapped from hg19 to hg38 using the UCSC liftover tool

323   (https://genome.ucsc.edu/cgi-bin/hgLiftOver).

324   For analysis of H3K27 acetylation in lung cancer at lineage-enriched candidate

325   regulatory elements, fastq files were generated from sequence read archives (SRA) from

326   published ChIP-seq experiments for SCLC[51] and LUAD[52-55] (SRA numbers SRR568435,

327   SRR3098556, SRR4449027, SRR4449025, and SRR6124068).

328   For Fig. 5c, H3K27ac ChIP-seq peaks from primary peripheral blood monocytes

329   (ENCFF540CVX) and epithelial keratinocytes (ENCFF943CBQ)[53] were used as a comparator to

330   peaks derived from LuCaP PDXs. For these comparisons, monocyte and keratinocyte peaks

331   within 1kb of a LuCaP peak were excluded.

332

333   **RNA-seq and differential expression analysis**

334   RNA-seq data from human adenocarcinoma and NEPC have been reported previously[8]

335   and were obtained from dbGaP (accession number phs000909.v1.p1). Transcriptomes were

336   sequenced from two replicates from each of five PRAD LuCaP PDXs (23, 77, 78, 81, and 96)

337   and five NEPC LuCaP PDXs (49, 93, 145.1, 145.2, and 173.1). RNA concentration, purity, and

338   integrity were assessed by NanoDrop (Thermo Fisher Scientific Inc.) and Agilent Bioanalyzer.

339   RNA-seq libraries were constructed from 1 µg total RNA using the Illumina TruSeq Stranded

10

340   mRNA LT Sample Prep Kit according to the manufacturer's protocol. Barcoded libraries were

341   pooled and sequenced on the Illumina HiSeq 2500 generating 50 bp paired end reads. FASTQ

342   files were processed using the VIPER workflow[56]. Read alignment to human genome build hg19

343   was performed with STAR[57]. Cufflinks was used to assemble transcript-level expression data

344   from filtered alignments[58]. Differential gene expression analysis (NEPC *vs*. PRAD) was

345   conducted using DESeq2[48].

346

347   **H3K27ac HiChIP**

348   Pulverized frozen tissue from LuCaP 173.1 was fixed with 1% formaldehyde in PBS at

349   room temperature for 10 minutes as previously described[38]. Sample was incubated in lysis

350   buffer and digested with MboI (NEB) for 4 hours. After 1 hour of biotin incorporation with biotin

351   dATP, the sample was ligated using T4 DNA ligase for 4 hours. Chromatin was sheared using

352   140 PIP, 5% duty cycle, and 200 cycles/burst for 8 minutes in shearing buffer composed of 1%

353   NP-40, 0.5% sodium deoxycholate, and 0.1% SDS in PBS (LNCaP) or using 100 PIP, 5% duty

354   cycle, 200 cycles/burst for 3 minutes in 1% SDS, 50mM Tris (pH 8.1), and 5mM EDTA (LuCaP

355   173.1). ChIP was then performed using H3K27Ac antibody (Diagenode, C1541019)[59].

356   Immunoprecipitated sample was pulled down with streptavidin C1 beads (Life

357   Technologies) and treated with Transposase (Illumina). Amplification was performed for the

358   number of cycles required to reach 1/3 of the maximal fluorescence on qPCR plot with SYBR®

359   Green I(Life Technologies). Libraries were sequenced using 150-base paired end reads on the

360   Illumina platform (Novogene).

361

362   *Alignment and filtering using HiC-Pro*

363   We processed paired-end fastq files using HiC-Pro[60] to generate intra- and inter-

364   chromosomal contact maps. The reads were first trimmed to remove adaptor sequences using

365   Trim Galore (*https://github.com/FelixKrueger/TrimGalore*). Default settings from HiC-Pro were

366   used to align reads to the hg19 human genome, assign reads to MboI restriction fragments, and

367   remove duplicate reads. Only uniquely mapped valid read pairs involving two different restriction

368   fragments were used to build the contact maps.

369

370   *FitHiChIP*

371   We applied FitHiChIP[61] for bias-corrected peak calling and DNA loop calling.

372   We used MACS2 broadPeak peak calls from H3K27ac ChIP-seq in LuCaP 173.1 (NEPC).

373   44,609 peaks were called at a q-value < 0.01. We used a 5Kb resolution and considered only

11

374   interactions between 5kb-3Mb. We used peak-to-peak (stringent) interactions for the global

375   background estimation of expected counts (and contact probabilities for each genomic

376   distance), and peak-to-all interactions for the foreground, meaning at least one anchor must

377   overlap a H3K27ac peak. The corresponding FitHiChiP options specified are "IntType=3" and

378   "UseP2PBackgrnd=1".

379

380   *Assignment of enhancer-promoter interactions using H3K27ac HiChIP data*

381   NCBI RefSeq genes (hg19) were downloaded from the UCSC genome table browser

382   (https://genome.ucsc.edu/cgi-bin/hgTables). Only uniquely mapping genes were considered.

383   The longest transcript was selected for genes with multiple annotated transcripts. We searched

384   for H3K27ac HiChIP loops with one anchor (defined with a 5kb window) overlapping a region

385   between 0 and 5kb upstream of a gene transcriptional start site. We selected subset of these

386   loops for which the second anchor (with a 5kb window) overlapped with H3K27ac peaks

387   identified by ChIP-seq in LuCaP 173.1 (NEPC) or with NEPC-enriched H3K27ac peaks (Ne-

388   CREs). Gene promoters and distal H3K27ac peaks / Ne-CREs were considered looped if each

389   overlapped with an anchor of the same high-confidence H3K27ac HiChIP loop(s). To examine

390   the association of regulatory element looping with gene expression, genes were binned by the

391   number of distinct, looped Ne-CREs or H3K27ac peaks. Differential expression between NEPC

392   and PRAD LuCaP PDXs, as assessed by DESeq2 analysis of LuCaP RNA-seq data, was

393   plotted for genes in each bin. Wilcoxon rank-sum *p*-values were calculated for differential

394   expression of genes looped to one versus two or more H3K27ac/Ne-CRE peaks. A *p*-value <

395   0.01 was considered significant.

396

397   **Master transcription factor analysis**

398   *Super-enhancer ranking analyses*

399   Enhancer and super-enhancer (SE) calls were obtained using the Rank Ordering of

400   Super-enhancer (ROSE2) algorithm[12]. We selected SEs assigned to transcription factors

401   (TFs)[62,63], and for each sample, we obtained the ranks of all TF SEs. Considering only the top

402   5% TFs by median ranking in NEPC or PRAD, we applied a one-sided Mann–Whitney U test to

403   identify lineage-enriched TF SEs (FDR = 10%).

404

405   *Clique enrichment and clustering analysis*

406   Clique enrichment scores (CESs) for each TF were calculated using clique assignments

407   from Coltron[64]. Coltron assembles transcriptional regulatory networks (cliques) based on H3K27

408   acetylation and TF binding motif analysis. The clique enrichment score for a given TF is the

409   number of cliques containing the TF divided by the total number of cliques. We incorporated

410   ATAC-seq data to restrict the motif search to regions of open chromatin. Using the CES, we

411   performed clustering (distance = Canberra, agglomeration method = ward.D2) considering only

412   TFs that appear in cliques in at least 80% of the samples in at least one lineage group (4 out of

413   5 NEPC and 11 out of 14 PRAD).

414

415   *Motif enrichment at super-enhancers with loops to the* FOXA1 *locus*

416   H3K27ac HiChIP data were used to select distal SEs that form three-dimensional

417   contacts with the *FOXA1* locus. We used the Coltron algorithm to search for TF motifs in ATAC-

418   seq peaks within these SEs. We considered all TFs that were categorized as expressed by

419   Coltron based on H3K27ac levels at the TF gene locus. Motif enrichment for a TF was

420   calculated as the total number of non-overlapping base pairs (bp) covered by the TF motif,

421   divided by the summed length (in bp) of the SEs. Values in the heatmap legend correspond to

422   percent coverage (i.e., the largest value corresponds to 0.4%).

423

424   **FOXA1 mutational profiling**

425   *FOXA1* mutational status was assessed from exome sequence data (62x-110X depth of

426   coverage). Each LuCaP PDX was sequenced using the Illumina Hi-seq platform with 100 bp

427   paired-end reads. Hybrid capture was performed SeqCapV3. Mouse genome subtraction was

428   performed using the mm10 genome build and reads were aligned to human reference genome

429   hg19. For sequence analysis, bam files processed as per Genome Analysis Toolkit (GATK) best

430   practice guideline[65]. Mutation pathogenicity was annotated using Clinvar, OncoKb and Civic. We

431   Used MuTect1 and Unified Genotyper for mutation calls. Copy number was derived using the

432   Sequenza R package.

433

434   **FOXA1 siRNA knock-down**

435   WCM154 organoids were cultured and maintained as previously described[19]. Organoids

436   were dissociated to single cells using TrypLE (ThermoFisher). One million cells were

437   resuspended in 20µl of electroporation buffer (BTXpress) and mixed with 60 pmole of control or

438   FOXA1 On-target pool siRNA (Dharmacon). Then organoid-siRNA mixtures were transferred to

439   a 16-well NucleocuvetteTM Strip and nucleofection was performed in a 4D-Nucleofector

440   (Lonza). Following nucleofection, 10^5 organoids cells were grown in a 12-well plate coated with

441   1% collagen I (ThermoFisher) for 7 days. Both adherent and floating cells were collected and

13

442 stained with 0.4% trypan blue solution (ThermoFisher). Total cell numbers were measured by a

443 hemocytometer. Cell proliferation with FOXA1 knock-down was normalized to control siRNA

444 cells.

445

446 **FOXA1 shRNA knock-down**

447 LNCaP, LNCaP 42D, and LNCaP 42F cells were seeded in parallel 6-well plates at

448 500k, 500k, or 100k, respectively. 24 hours later, cells were infected with lentivirus containing

449 shRNAs targeting GFP control or *FOXA1*. 48 hours following infection, equal cell numbers were

450 seeded, and proliferation was assayed 6 days later using a Vi-Cell. 72 hours following infection,

451 a second plate infected in parallel was harvested for immunoblotting. The target sequence

452 against GFP was CCACATGAAGCAGCACGACTT (shGFP). The target sequences against

453 FOXA1 were GCGTACTACCAAGGTGTGTAT (shFOXA1-1) and

454 TCTAGTTTGTGGAGGGTTAT (shFOXA1-2).

455

456 **FOXA1 CRISPR-Cas9 knock-out**

457 Blasticidin-resistant Cas9 positive LNCaP, LNCaP 42D, and LNCaP 42F cells were

458 cultured in 20µg/mL blasticidin (Thermo Fisher Scientific, NC9016621) for 72 hours to select for

459 cells with optimal Cas9 activity. LNCaP, LNCaP 42D, and LNCaP 42F, PC3M cells were seeded

460 in parallel 6-well plates at 300k, 300k, 300k, or 60k, respectively. Cells were infected after 24

461 hours with lentiviruses expressing sgRNAs targeting GFP control or *FOXA1*. Cells were subject

462 to puromycin selection and harvested for immunoblot after 3 days. 6 days following selection,

463 cell viability was determined using a Vi-Cell. The target sequences against GFP were

464 AGCTGGACGGCGACGTAAA (sgGFP1) and GCCACAAGTTCAGCGTGTCG (sgGFP2). The

465 target sequences against FOXA1 were GTTGGACGGCGCGTACGCCA (sgFOXA1-1),

466 GTAGTAGCTGTTCCAGTCGC (sgFOXA1-2), CAGCTACTACGCAGACACGC (sgFOXA1-3),

467 and ACTGCGCCCCCATAAGCTC (sgFOXA1-4).

468

469 **Western Blots**

470 For WCM154 Western blots, cell pellets were lysed in RIPA buffer (MilliporeSigma, 20-

471 188) supplemented with Protease/Phosphatase Inhibitor Cocktail (Cell Signaling Technology,

472 5872S). Protein concentrations were assayed with a Pierce BCA Protein Assay Kit (Thermo

473 Fisher Scientific, PI23225), and protein was subsequently denatured in NuPAGE LDS sample

474 buffer (Thermo Fisher Scientific, NP0007) containing 5% β-Mercaptoethanol. 13µg of each

475 protein sample was loaded onto NuPAGE 4-12% Bis-Tris Protein gels (Thermo Fisher

14

476   Scientific), and samples were run in NuPAGE MOPS SDS Running Buffer (Thermo Fisher

477   Scientific, NP0001). Following electrophoresis, proteins were transferred to nitrocellulose

478   membranes via an iBlot apparatus (Thermo Fisher Scientific). After blocking in Odyssey

479   Blocking Buffer (LI-COR Biosciences, 927-70010) for one hour at room temperature,

480   membranes were cut and incubated in primary antibodies diluted 1:1000 in Odyssey Blocking

481   Buffer overnight at 4°C. The next morning, membranes were washed three times with

482   Phosphate-Buffer Saline, 0.1% Tween (PBST) and then incubated with fluorescent anti-rabbit

483   secondary antibodies (Thermo Fisher Scientific, NC9401842) for one hour at room temperature.

484   Membranes underwent five PBST washes and were then imaged using an Odyssey Imaging

485   System (LI-COR Biosciences). Primary antibodies used include FOXA1 (Cell Signaling

486   Technology, 58613S) and β-actin (Cell Signaling Technology, 8457L).

487   For LNCaP, LNCaP 42D, and LNCaP 42F Western Blots, cell lysate was extracted using

488   RIPA lysis buffer (Sigma) containing protease inhibitor (Roche) and phosphatase inhibitor

489   (ThermoFisher). 50 µg of protein was subjected to a 4-15% Mini-PROTEAN Precast

490   electrophoresis gel (Bio-Rad) then transferred to 0.22 um nitrocellulose membrane (Bio-Rad)

491   and blocked in 5% blotting grade blocker (Bio-Rad). Membranes were incubated with primary

492   antibodies overnight (FOXA1, Abcam, 1:2000, ab23738; Synaptophysin, Cell Marque, 1:5000,

493   MRQ-40; INSM1, Santa Cruz, 1:2000, sc-377428; FOXA2, Abcam; 1:2500, ab108422;

494   Chromogranin A, Abcam, 1:2000, ab15160; Vinculin Cell signaling, 1:5000, #13901).

495   Membranes were then washed in 1x Tris-buffered saline with 0.5% Tween-20 (Boston

496   BioProducts) and incubated with secondary antibodies (mouse, Bio-Rad, 1:2500; rabbit, Bio-

497   Rad, 1:2500). Western HRP substrate kit was used to detect chemiluminescent signal (Millipore,

498   Classico).

499

500   **Analysis of FOXA1 binding sites across prostate cancer states**

501   FOXA1 cistromes were compared across different states of prostate cancer progression

502   (normal prostate, prostate-localized adenocarcinoma, PDXs derived from metastatic castration

503   resistant prostate cancer, and PDXs derived from NEPC). FOXA1 ChIP from normal prostate

504   tissue and prostate-localized adenocarcinoma will be reported separately (Pomerantz *et al.*,

505   submitted). For normal prostate tissue FOXA1 ChIP, tissue cores were obtained from regions of

506   prostatectomy specimens with dense epithelium and no evidence of neoplasia on review by a

507   genitourinary pathologist. PDX samples used are listed in Table S1. PDXs derived from

508   localized prostate cancer were excluded from this analysis. Because the normal prostate and

509   localized adenocarcinoma samples were sequenced with single-end sequencing with an

15

510 average of ~20 million reads, paired-end sequencing data from LuCaP PDXs were down-

511 sampled to 20M reads, using a single end trimmed to 75 base-pairs using seqtk

512 (https://github.com/lh3/seqtk).

513 Pairwise comparisons were made between normal prostate (N=5) and localized PRAD

514 (N=5), localized PRAD and metastatic PRAD PDXs (N=11), and metastatic PRAD PDXs and

515 NEPC PDXs (N=5) using DESeq2 as described above. Peaks were considered significantly

516 different between groups at a log2 |fold-change| threshold of 2 and FDR-adjusted *p*-value

517 threshold of 0.001. "Shared" peaks were defined as the intersection of all peaks that were

518 present in each group but not significantly different in any comparison.

519

520 **Immunohistochemistry**

521 Immunohistochemistry was performed on tissue microarray (TMA) sections. TMA slides

522 were stained for FOXA1 (Abcam ab170933, 1:100 dilution with 10 mM NaCitrate antigen

523 retrieval) and FOXA2 (Abcam ab108422, 1:500 dilution with 10 mM NaCitrate antigen retrieval)

524 using a standard procedure[66]. Rabbit IgG was used as a negative control. Nuclear staining

525 intensity was assigned levels 0, 1+, 2+, or 3+ and H-scores were calculated as: [1 x (% of 1+

526 cells) + 2 x (% of 2+ cells) + 3 x (% of 3+ cells)]. Evaluations were performed in a blinded

527 fashion.

528

529 **ASCL1/NKX2-1 overexpression in LNCaP**

530 *Transduction of LNCaP cells with ASCL1 and NKX2-1*

531 The open reading frames of ASCL1 and NKX2-1 were cloned into the pLX_TRC302

532 lentiviral expression vector (Broad Institute) using the gateway recombination system. A

533 construct expressing eGFP (pLX_TRC302_GFP) was used as a negative control. Viruses were

534 generated by transfecting 293T cells with packaging vectors pVsVg and pDelta8.9. Supernatant

535 was collected after 48 hours. LNCaP cells were transduced in the presence of 4µg/ml polybrene

536 and harvested after 3 days for RNA-seq, ATAC-seq, and ChIP-seq.

537 ChIP seq was performed as described above, using 10-15 million cells fixed with 1%

538 paraformaldehyde for 10 minutes at room temperature, followed by quenching with glycine.

539 RNA was isolated using QIAGEN RNeasy Plus Kit and cDNA synthesized using Clontech RT

540 Advantage Kit. Quantitative PCR was performed on a Quantstudio 6 using SYBR green. The

541 following primers were used for qRT-PCR:

AR qRT-PCR fwd	GTGTCAAAAGCGAAATGGGC
AR qRT-PCR rev	GCTTCATCTCCACAGATCAGG

16

ASCL1 qRT-PCR fwd	CTACTCCAACGACTTGAACTCC
ASCL1 qRT-PCR rev	AGTTGGTGAAGTCGAGAAGC
GAPDH qRT-PCR fwd	CATGAGAAGTATGACAACAGCCT
GAPDH qRT-PCR rev	AGTCCTTCCACGATACCAAAGT
SOX2 qRT-PCR fwd	CACACTGCCCCTCTCAC
SOX2 qRT-PCR rev	TCCATGCTGTTTCTTACTCTCC
SYP qRT-PCR fwd	AGACAGGGAACACATGCAAG
SYP qRT-PCR rev	TCTCCTTAAACACGAACCACAG

542 **Analysis of promoter H3K4 and H3K27 trimethylation**

543 Refseq gene coordinates (hg19) were compiled, selecting the longest isoform where

544 multiple were annotated. Normalized tag counts from H3K27me3 and H3K4me3 ChIP-seq

545 within 2kb of each transcriptional start site (TSS) were calculated for each sample, then

546 averaged across multiple samples in each group (five NEPC PDXs, five PRAD PDXs, three

547 normal prostates; Pomerantz et al., submitted). Contours were calculated using the R function

548 geom_density_2d from the ggplot2 package; they represent the 2d kernel density estimation for

549 all included transcriptional start sites. Gene promoters were assigned "active", "bivalent",

550 "unmarked", and "repressed" annotations based on H3K4me3 and H3K27me3 levels. High/low

551 cutoffs for these marks were determined as follows. First, the H3K4me3 normalized tag counts

552 near each TSS were fit to two normal distributions using the normalmixEM R function from the

553 mixtools R package. The cutoff between H3K4me3-high and -low was set at four standard

554 deviations below the mean value of the H3K4me3-high distribution. Next, the normalized

555 H3K27me3 tag counts near H3K4me3-high TSSs were fit to two normal distributions. The cutoff

556 for H3K27me3-high promoters was set at four standard deviations above the mean value of the

557 H3K27me3-low distribution. The Pearson Chi-squared test was used to quantify significance of

558 enrichment of NEPC-upregulated genes in the "bivalent" quadrant compared to "repressed" or

559 "unmarked" quadrants. NEPC-upregulated genes were defined as those with log_2 fold-change >

560 3 and adjusted *p*-value < 1×10^{-6} in NEPC *vs*. PRAD. The results of the analysis were robust to

561 using other *p*-value and differential expression thresholds.

562

563 **Methylation analysis of normal prostate**

564 Whole genome bisulfite sequencing data from histologically normal prostate tissue were

565 reported previously[67] and processed as previously described[68]. CpG methylation at indicated

566 sites was visualized using deepTools[46].

567

17

Data Availability:

Sequence data in fastq format from this study will be deposited in GEO. Requests for LuCaP PDXs should be directed to Dr. Eva Corey (ecorey@uw.edu)

Author contributions:

S.C.B. analyzed ChIP-seq data and wrote the manuscript. X.Q. assisted with ChIP-seq data analysis. D.Y.T., J.H., and T.A. performed ASCL1/NKX2-1 overexpression experiments. S.Y.K. performed FOXA1 siRNA experiments under supervision of H.B. J.H., T.A., R.A., and S.A. performed FOXA1 shRNA and CRISPR experiments. E.O., C.B., and S.A.A. performed ChIP-seq experiments. J.-H.S. performed HiChIP experiments. C.G and B.P analyzed HiChIP data. R.I.C and M.A.S.F. performed core regulatory analysis under supervision of K.L. P.C. and K.L. performed ATAC-seq under supervision of H.W.L. and M.B. M.H. and A.N. assisted with procurement of clinical samples. J.E.B. and K. K. assisted with analysis of WGBS methylation data. L.B. performed immunohistochemistry experiments. I.M.C., and A.K. performed RNA-seq under the supervision of P.S.N. H.H.N., C.M., and E.C. provided LuCaP PDXs. E.C., M.M.P. and M.L.F. supervised the project.

Competing interests statement: W.C.H. is a consultant for Thermo Fisher, Solasta Ventures, iTeos, Frontier Medicines, Tyra Biosciences, MPM Capital, KSQ Therapeutics, and Paraxel and is a founder of KSQ Therapeutics.

18

References:

1. Aggarwal, R. *et al.* Clinical and genomic characterization of treatment-emergent small-cell neuroendocrine prostate cancer: a multi-institutional prospective study. *J. Clin. Oncol.* **36**, 2492–2503 (2018).

2. Sequist, L. V. *et al.* Genotypic and histological evolution of lung cancers acquiring resistance to EGFR inhibitors. *Sci. Transl. Med.* **3**, 75ra26 (2011).

3. Zaret, K. S. & Carroll, J. S. Pioneer transcription factors: establishing competence for gene expression. *Genes Dev.* **25**, 2227–2241 (2011).

4. Friedman, J. & Kaestner, K. The Foxa family of transcription factors in development and metabolism. *Cell. Mol. Life Sci.* **63**, 2317–28 (2006).

5. Scher, H. *et al.* Increased survival with enzalutamide in prostate cancer after chemotherapy. *N. Engl. J. Med* **367**, 1187–1197 (2012).

6. de Bono, J. S. *et al.* Abiraterone and increased survival in metastatic prostate cancer. *N. Engl. J. Med.* **364**, 1995–2005 (2011).

7. Bluemn, E. *et al.* Androgen Receptor pathway-independent prostate cancer is sustained through FGF signaling. *Cancer Cell* **32**, 474-489.e6 (2017).

8. Beltran, H. *et al.* Divergent clonal evolution of castration resistant neuroendocrine prostate cancer. *Nat. Med.* **22**, 298–305 (2016).

9. Davies, A. H., Beltran, H. & Zoubeidi, A. Cellular plasticity and the neuroendocrine phenotype in prostate cancer. *Nat. Rev. Urol.* **15**, 271–286 (2018).

10. Nguyen, H. *et al.* LuCaP prostate cancer patient-derived xenografts reflect the molecular heterogeneity of advanced disease and serve as models for evaluating cancer therapeutics. *Prostate* **77**, 654–671 (2017).

11. Mu, P. *et al.* SOX2 promotes lineage plasticity and antiandrogen resistance in TP53- and RB1-deficient prostate cancer. *Science* **355**, 84–88 (2017).

12. Whyte, W. A. *et al.* Master transcription factors and mediator establish super-enhancers at key cell identity genes. *Cell* **153**, 307–319 (2013).

13. Lin, C. *et al.* Active medulloblastoma enhancers reveal subgroup-specific cellular origins. *Nature* **530**, 57 (2016).

14. Ott, C. J. *et al.* Enhancer architecture and essential core regulatory circuitry of chronic lymphocytic leukemia. *Cancer Cell* **34**, 982-995.e7 (2018).

15. Qi, J. *et al.* Siah2-dependent concerted activity of HIF and FoxA2 regulates formation of neuroendocrine phenotype and neuroendocrine prostate tumors. *Cancer Cell* **18**, 23–38 (2010).

19

630   16. Parolia, A. *et al.* Distinct structural classes of activating FOXA1 alterations in advanced
631   prostate cancer. *Nature* **571**, 413–418 (2019).

632   17. Jaenisch, R. & Young, R. Stem cells, the molecular circuitry of pluripotency and nuclear
633   reprogramming. *Cell* **132**, 567–582 (2008).

634   18. Bishop, J. L. *et al.* The master neural transcription factor BRN2 is an Androgen Receptor-
635   suppressed driver of neuroendocrine differentiation in prostate cancer. *Cancer Discov.* **7**,
636   54–71 (2017).

637   19. Puca, L. *et al.* Patient derived organoids to model rare prostate cancer phenotypes. *Nat.*
638   *Commun.* **9**, 2404 (2018).

639   20. Donaghey, J. *et al.* Genetic determinants and epigenetic effects of pioneer-factor
640   occupancy. *Nat. Genet.* **50**, 250–258 (2018).

641   21. Ousset, M. *et al.* Multipotent and unipotent progenitors contribute to prostate postnatal
642   development. *Nat. Cell. Biol.* **14**, 1131 (2012).

643   22. Pignon, J.-C. *et al.* p63-expressing cells are the stem cells of developing prostate, bladder,
644   and colorectal epithelia. *Proc. Natl. Acad. Sci.* **110**, 8105–8110 (2013).

645   23. Hon, G. C. *et al.* Epigenetic memory at embryonic enhancers identified in DNA methylation
646   maps from adult mouse tissues. *Nat. Genet.* **45**, 1198–1206 (2013).

647   24. Jadhav, U. *et al.* Extensive recovery of embryonic enhancer and gene memory stored in
648   hypomethylated enhancer DNA. *Mol. Cell* **74**, 542-554.e5 (2019).

649   25. Bernstein, B. E. *et al.* A bivalent chromatin structure marks key developmental genes in
650   embryonic stem cells. *Cell* **125**, 315–26 (2006).

651   26. Jadhav, U. *et al.* Acquired tissue-specific promoter bivalency is a basis for PRC2 necessity
652   in adult cells. *Cell* **165**, 1389–1400 (2016).

653   27. Mohn, F. *et al.* Lineage-specific polycomb targets and de novo DNA methylation define
654   restriction and potential of neuronal progenitors. *Mol. Cell* **30**, 755–766 (2008).

655   28. Schoenherr, C. & Anderson, D. The neuron-restrictive silencer factor (NRSF): a coordinate
656   repressor of multiple neuron-specific genes. *Science* **267**, 1360–3 (1995).

657   29. Park, J. *et al.* Reprogramming normal human epithelial tissues to a common, lethal
658   neuroendocrine cancer lineage. *Science* **362**, 91–95 (2018).

659   30. Ku, S. *et al.* Rb1 and Trp53 cooperate to suppress prostate cancer lineage plasticity,
660   metastasis, and antiandrogen resistance. *Science* **355**, 78–83 (2017).

661   31. Kim, J. *et al.* FOXA1 inhibits prostate cancer neuroendocrine differentiation. *Oncogene* **36**,
662   4072–4080 (2017).

663 32. Borromeo, M. D. *et al.* ASCL1 and NEUROD1 reveal heterogeneity in pulmonary
664   neuroendocrine tumors and regulate distinct genetic programs. *Cell. Rep.* **16**, 1259–1272
665   (2016).

666 33. Balanis, N. G. *et al.* Pan-cancer convergence to a small-cell neuroendocrine phenotype that
667   shares susceptibilities with hematological malignancies. *Cancer Cell* **36**, 17-34.e7 (2019).

668 34. Beshiri, M. L. *et al.* A PDX/organoid biobank of advanced prostate cancers captures
669   genomic and phenotypic heterogeneity for disease modeling and therapeutic screening.
670   *Clin. Cancer Res.* **24**, 4332–4345 (2018).

671 35. Gleave, A. M., Ci, X., Lin, D. & Wang, Y. A synopsis of prostate organoid methodologies,
672   applications, and limitations. *The Prostate* **80**, 518–526 (2020).

673 36. Kanan, A. D., Corey, E., Vêncio, R. Z. N., Ishwar, A. & Liu, A. Y. Lineage relationship
674   between prostate adenocarcinoma and small cell carcinoma. *BMC Cancer* **19**, 518 (2019).

675 37. Labrecque, M. P. *et al.* Molecular profiling stratifies diverse phenotypes of treatment-
676   refractory metastatic castration-resistant prostate cancer. *J. Clin. Invest.* **129**, 4492–4505
677   (2019).

678 38. Pomerantz, M. M. *et al.* The androgen receptor cistrome is extensively reprogrammed in
679   human prostate tumorigenesis. *Nat. Genet.* **47**, 1346–1351 (2015).

680 39. Johnson, D. S., Mortazavi, A., Myers, R. M. & Wold, B. Genome-wide mapping of in vivo
681   protein-DNA interactions. *Science* **316**, 1497–1502 (2007).

682 40. Corces, M. R. *et al.* An improved ATAC-seq protocol reduces background and enables
683   interrogation of frozen tissues. *Nat. Methods* **14**, 959–962 (2017).

684 41. Buenrostro, J., Wu, B., Chang, H. & Greenleaf, W. ATAC-seq: A method for assaying
685   chromatin accessibility genome-wide. *Curr. Protoc. Mol. Biol.* **109**, 21.29.1-21.29.9 (2015).

686 42. Langmead, B., Trapnell, C., Pop, M. & Salzberg, S. L. Ultrafast and memory-efficient
687   alignment of short DNA sequences to the human genome. *Genome Biol.* **10**, R25 (2009).

688 43. Zhang, Y. *et al.* Model-based Analysis of ChIP-Seq (MACS). *Genome Biol.* **9**, R137 (2008).

689 44. Cavalcante, R. G. & Sartor, M. A. annotatR: genomic regions in context. *Bioinformatics* **33**,
690   2381–2383 (2017).

691 45. Robinson, J. T. *et al.* Integrative Genomics Viewer. *Nat. Biotechnol.* **29**, 24–26 (2011).

692 46. Ramírez, F., Dündar, F., Diehl, S., Grüning, B. A. & Manke, T. deepTools: a flexible platform
693   for exploring deep-sequencing data. *Nucleic Acids Res.* **42**, W187–W191 (2014).

694 47. Köster, J. & Rahmann, S. Snakemake—a scalable bioinformatics workflow engine.
695   *Bioinformatics* **28**, 2520–2522 (2012).

696 48. Love, M. I., Huber, W. & Anders, S. Moderated estimation of fold change and dispersion for
697   RNA-seq data with DESeq2. *Genome Biol.* **15**, 550 (2014).

698 49. McLean, C. Y. *et al.* GREAT improves functional interpretation of cis-regulatory regions.
699   *Nat. Biotechnol.* **28**, 495–501 (2010).

700 50. Layer, R. M. *et al.* GIGGLE: a search engine for large-scale integrated genome analysis.
701   *Nat. Methods* **15**, 123–126 (2018).

702 51. Huang, Y.-H. *et al.* POU2F3 is a master regulator of a tuft cell-like variant of small cell lung
703   cancer. *Genes Dev.* **32**, 915–928 (2018).

704 52. Abraham, B. J. *et al.* Small genomic insertions form enhancers that misregulate oncogenes.
705   *Nat. Commun.* **8**, 14385 (2017).

706 53. ENCODE Project Consortium. An integrated encyclopedia of DNA elements in the human
707   genome. *Nature* **489**, 57–74 (2012).

708 54. Rusan, M. *et al.* Suppression of adaptive responses to targeted cancer therapy by
709   transcriptional repression. *Cancer Discov.* **8**, 59–73 (2018).

710 55. Handoko, L. *et al.* JQ1 affects BRD2-dependent and independent transcription regulation
711   without disrupting H4-hyperacetylated chromatin states. *Epigenetics* **13**, 410–431 (2018).

712 56. Cornwell, M. *et al.* VIPER: Visualization Pipeline for RNA-seq, a Snakemake workflow for
713   efficient and complete RNA-seq analysis. *BMC Bioinformatics* **19**, 135 (2018).

714 57. Dobin, A. *et al.* STAR: ultrafast universal RNA-seq aligner. *Bioinformatics* **29**, 15–21 (2013).

715 58. Trapnell, C. *et al.* Differential gene and transcript expression analysis of RNA-seq
716   experiments with TopHat and Cufflinks. *Nat. Protoc.* **7**, 562–578 (2012).

717 59. Mumbach, M. R. *et al.* HiChIP: efficient and sensitive analysis of protein-directed genome
718   architecture. *Nat. Methods* **13**, 919–922 (2016).

719 60. Servant, N. *et al.* HiC-Pro: an optimized and flexible pipeline for Hi-C data processing.
720   *Genome Biol.* **16**, 259 (2015).

721 61. Bhattacharyya, S., Chandra, V., Vijayanand, P. & Ay, F. FitHiChIP: Identification of
722   significant chromatin contacts from HiChIP data. *bioRxiv* 412833 (2018)
723   doi:10.1101/412833.

724 62. D'Alessio, A. C. *et al.* A systematic approach to identify candidate transcription factors that
725   control cell identity. *Stem Cell Rep.* **5**, 763–775 (2015).

726 63. Lambert, S. A. *et al.* The human transcription factors. *Cell* **172**, 650–665 (2018).

727 64. Federation, A. J. *et al.* Identification of candidate master transcription factors within
728   enhancer-centric transcriptional regulatory networks. *bioRxiv* 345413 (2018)
729   doi:10.1101/345413.

730   65. Van der Auwera, G. A. *et al.* From FastQ data to high confidence variant calls: the Genome
731   Analysis Toolkit best practices pipeline. *Curr Protoc Bioinformatics* **43**, 11.10.1-11.10.33
732   (2013).
733   66. Nguyen, H. M. *et al.* Cabozantinib inhibits growth of androgen-sensitive and castration-
734   resistant prostate cancer and affects bone remodeling. *PLoS ONE* **8**, e78881 (2013).
735   67. Yu, Y. P. *et al.* Whole-genome methylation sequencing reveals distinct impact of differential
736   methylations on gene transcription in prostate cancer. *Am. J. Pathol.* **183**, 1960–1970
737   (2013).
738   68. Takeda, D. Y. *et al.* A somatically acquired enhancer of the Androgen Receptor is a
739   noncoding driver in advanced prostate cancer. *Cell* **174**, 422-432.e13 (2018).
740   69. Tsherniak, A. *et al.* Defining a cancer dependency map. *Cell* **170**, 564-576.e16 (2017).
741   70. Henry, G. H. *et al.* A cellular anatomy of the normal adult human prostate and prostatic
742   urethra. *Cell Rep.* **25**, 3530-3542.e5 (2018).
743
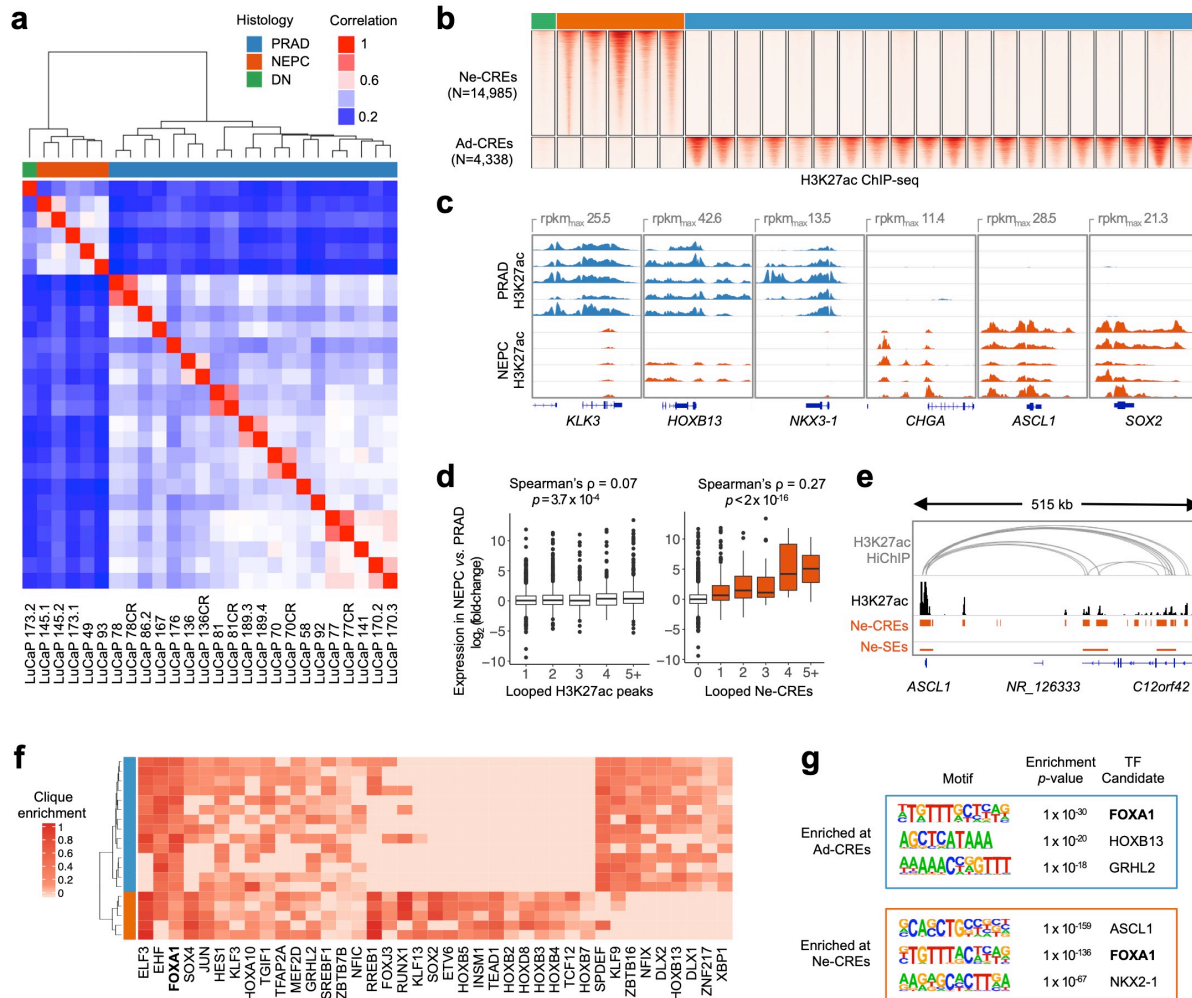
Figure 1. Epigenomic divergence of PRAD and NEPC. a, Hierarchical clustering of PRAD and NEPC based on sample-to-sample correlation of H3K27ac profiles. "DN" ("double-negative") indicates a LuCaP PDX without AR or NE marker expression (see also Supplementary Figure 1). **b**, Heatmaps of normalized H3K27ac tag densities at differentially H3K27-acetylated regions (±2kb from peak center) between NEPC and PRAD. "CREs" signify candidate regulatory elements. **c**, H3K27ac signal near selected prostate-lineage and NEPC genes. Five representative samples from each histology are shown. **d**, Differential expression (NEPC *vs*. PRAD) of genes with the indicated number of distinct looped H3K27ac peaks (left) or Ne-CREs (right) detected by H3K27ac HiChIP in LuCaP 173.1 (NEPC). Wilcoxon *p*-value is indicated for comparison of genes with loops to one Ne-CRE or H3K27ac peak versus two or more. **e**, H3K27ac HiChIP loops in LuCaP 173.1 from *ASCL1* to Ne-CREs and NEPC-restricted super-enhancers (Ne-SEs). H3K27ac tag density for LuCaP 173.1 is shown in black. **f**, Candidate master transcription factors in NEPC and PRAD based on regulatory clique enrichment (see methods). **g**, Three most significantly enriched nucleotide motifs present in >10% of Ad-CREs or Ne-CREs by *de novo* motif analysis.

1
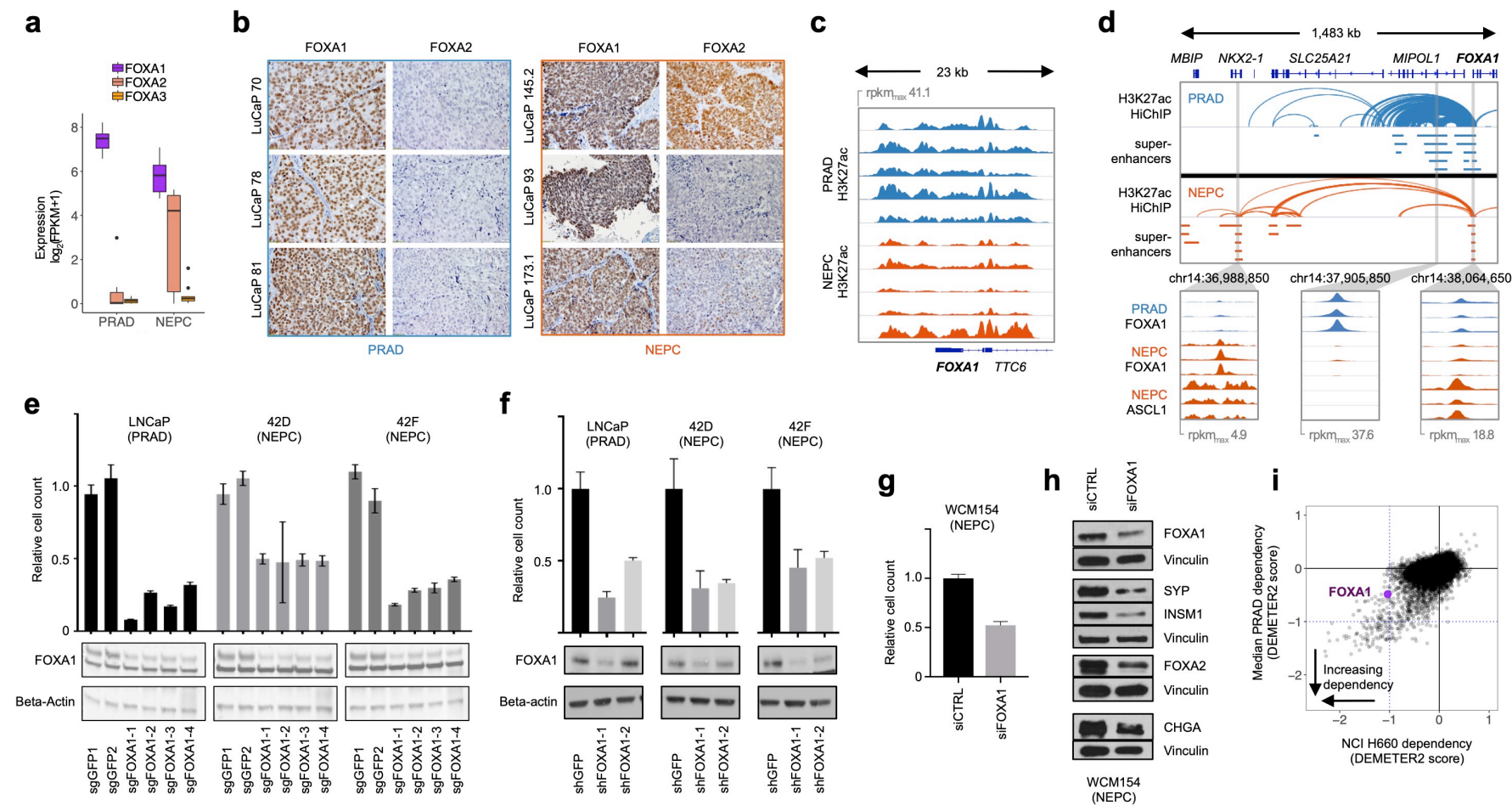
Figure 2. FOXA1 remains a critical lineage transcription factor in NEPC. a, Transcript expression of FOXA family TFs in LuCaPs PDXs (5 NEPC and 5 PRAD; 2 replicates each). **b**, FOXA1/FOXA2 immunohistochemistry in six representative PDXs. **c**, H3K27ac profiles at *FOXA1* in five representative PRAD and NEPC PDXs. **d**, H3K27ac HiChIP loops near *FOXA1* in LuCaP 173.1 (NEPC) and LNCaP (PRAD). Bars indicate super-enhancers in five representative LuCaPs of each lineage. Blowups show ChIP-seq read pileups for FOXA1 and ASCL1 in PDXs of the indicated lineage. **e-f**, Proliferation of LNCaP and 42D/42F derivatives with inactivation of FOXA1 by CRISPR (e) or shRNA (f). **g-h**, Proliferation (g) and expression of neuroendocrine marker proteins (h) with siRNA knock-down of FOXA1 in the NEPC organoid model WCM154. **i**, Essentiality of genes in NCI-H660 (NEPC) versus PRAD cell lines in a published shRNA screening dataset[69]. More negative DEMETER2 scores indicate greater dependency. The blue lines indicate the median DEMETER2 score for pan-essential genes.
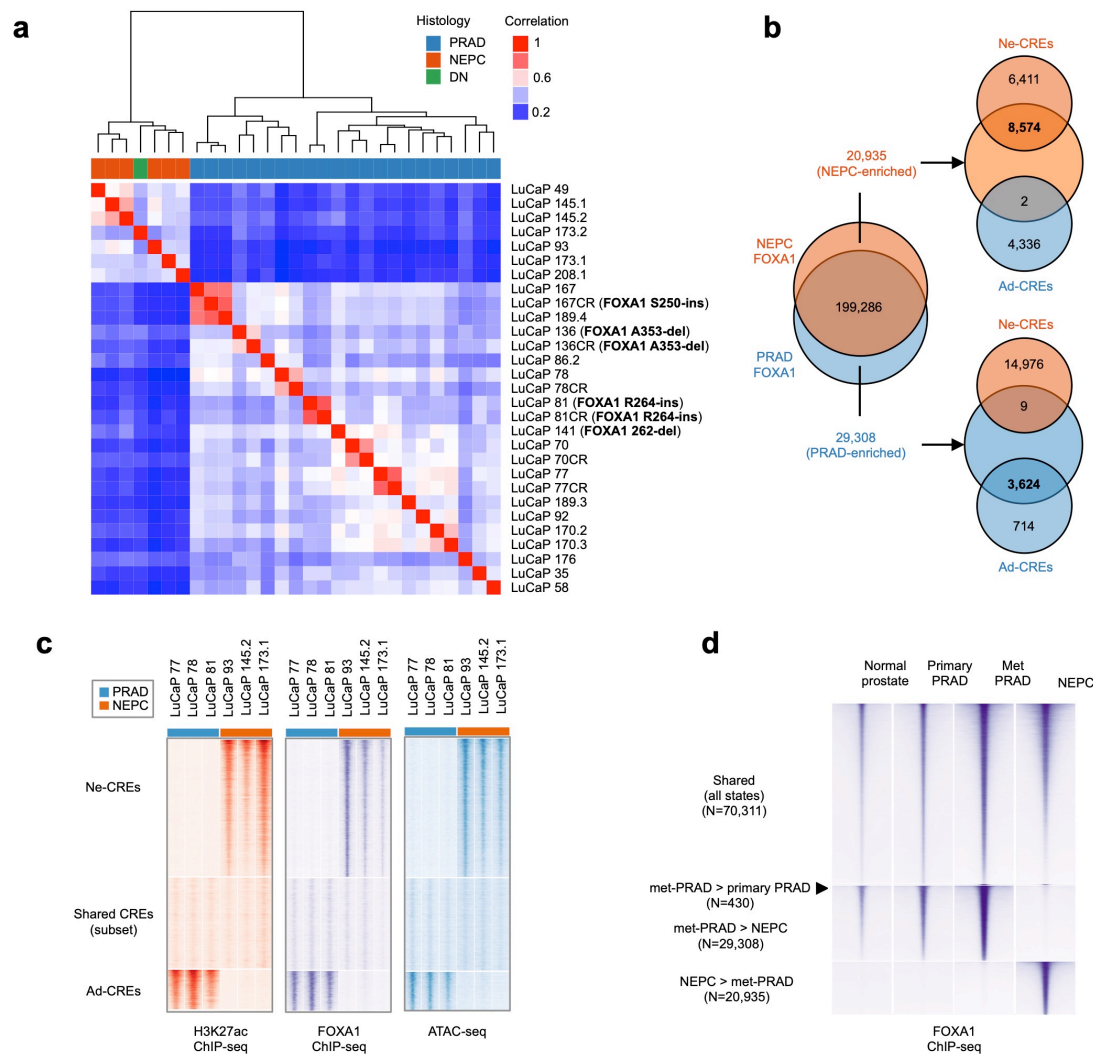
Figure 3. Reprogramming of the FOXA1 cistrome in NEPC. a, Hierarchical clustering of LuCaP PDXs by FOXA1 binding profiles. "DN" ("double-negative") indicates a PDX without AR or NE marker expression. FOXA1 mutational status is noted; see also Table S7) **b**, Venn diagram of lineage-enriched and shared FOXA1 binding sites and their overlap with lineage-enriched candidate regulatory elements (Ad-CREs and Ne-CREs). **c**, Normalized tag densities for H3K27ac/FOXA1 ChIP-seq and ATAC-seq at Ne-CREs and Ad-CREs. Three representative NEPC and PRAD PDXs are shown. **d**, Average normalized tag densities for FOXA1 in normal prostate, primary PRAD, and PDXs derived from PRAD metastases (Met PRAD) or NEPC (five samples in each category) at differential FOXA1 binding sites between these groups. There are insufficient differential sites to display (<100) for the Primary PRAD > Met PRAD comparison and the Primary PRAD *vs*. Normal prostate comparisons.

3
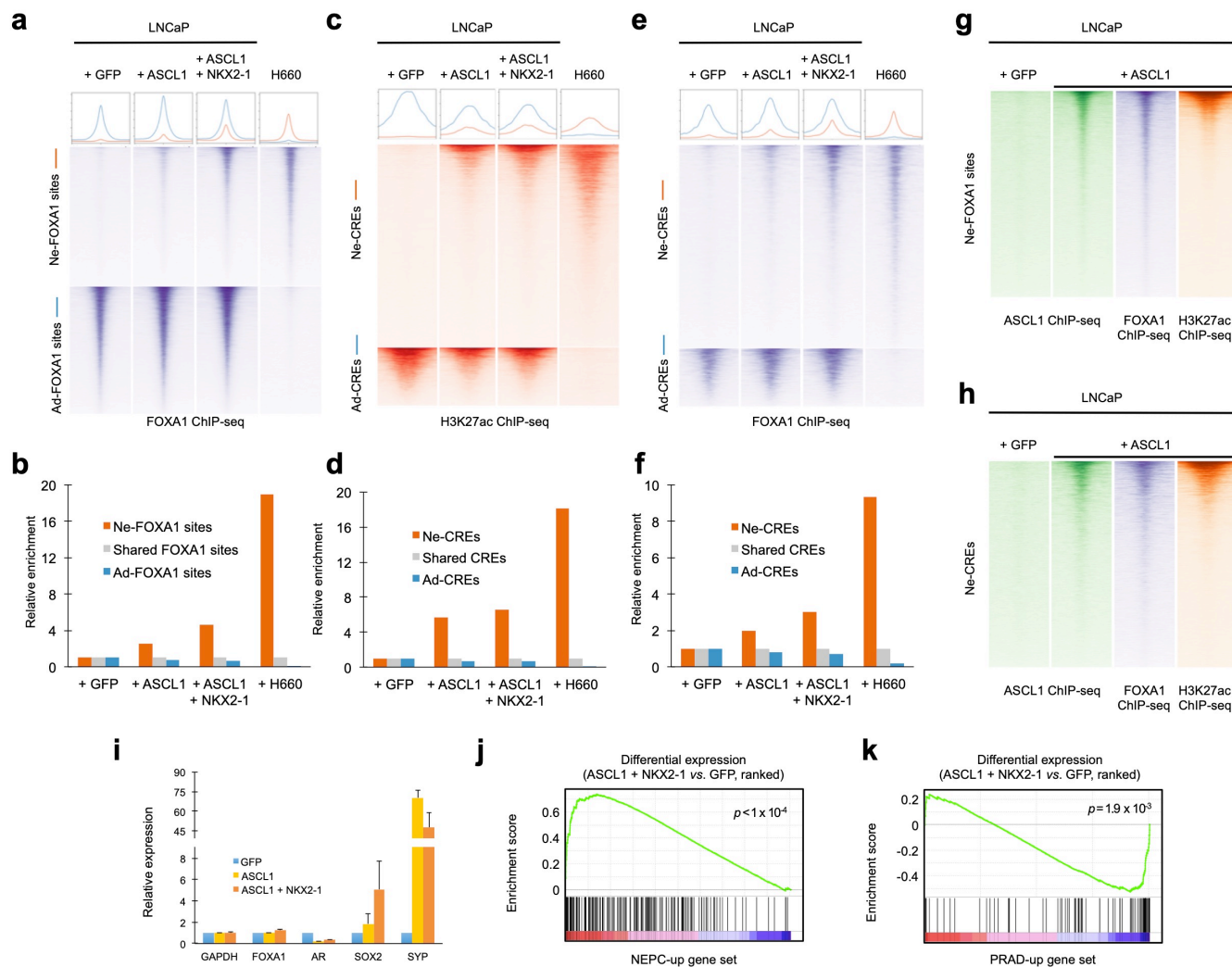
Figure 4. FOXA1 is extensively redistributed at lineage-specific regulatory elements. a, Normalized ChIP-seq tag density for FOXA1 at NEPC-enriched and PRAD-enriched FOXA1 binding sites under the indicated conditions. Profile plots (top) represent mean tag density at sites depicted in the heatmaps. **b**, Enrichment of FOXA1 peaks for overlap with NEPC-enriched and PRAD-enriched FOXA1 binding sites in the indicated conditions, normalized to FOXA1 peaks shared between PRAD and NEPC. **c-f**, Normalized ChIP-seq tag density for H3K27ac (c) and FOXA1 (e) at Ne-CREs and Ad-CREs under the indicated experimental conditions. Enrichment of overlap of H3K27ac peaks (d) and FOXA1 peaks (f) with Ne-CREs and Ad-CREs under the indicated conditions. **g-h** Normalized ChIP-seq tag density for ASCL1, FOXA1, and H3K27ac under the indicate experimental conditions at NEPC-enriched FOXA1 sites (g) and Ne-CREs (h). **i**, Effect of ASCL1 overexpression on transcript levels of indicated genes, measured by qPCR. Fold-change relative to +GFP condition is shown, using normalization to GAPDH. The average of three biological replicates is shown for each condition. Error bars represent standard deviation. **j-k**, Gene set enrichment analysis of genes upregulated at least 8-fold in LuCaP NEPC (j) or PRAD (k) at adjusted p-value < 10^{-18}. Genes are ranked by differential expression between LNCaP + ASCL1 + NKX2-1 and + GFP conditions based on RNA-seq.
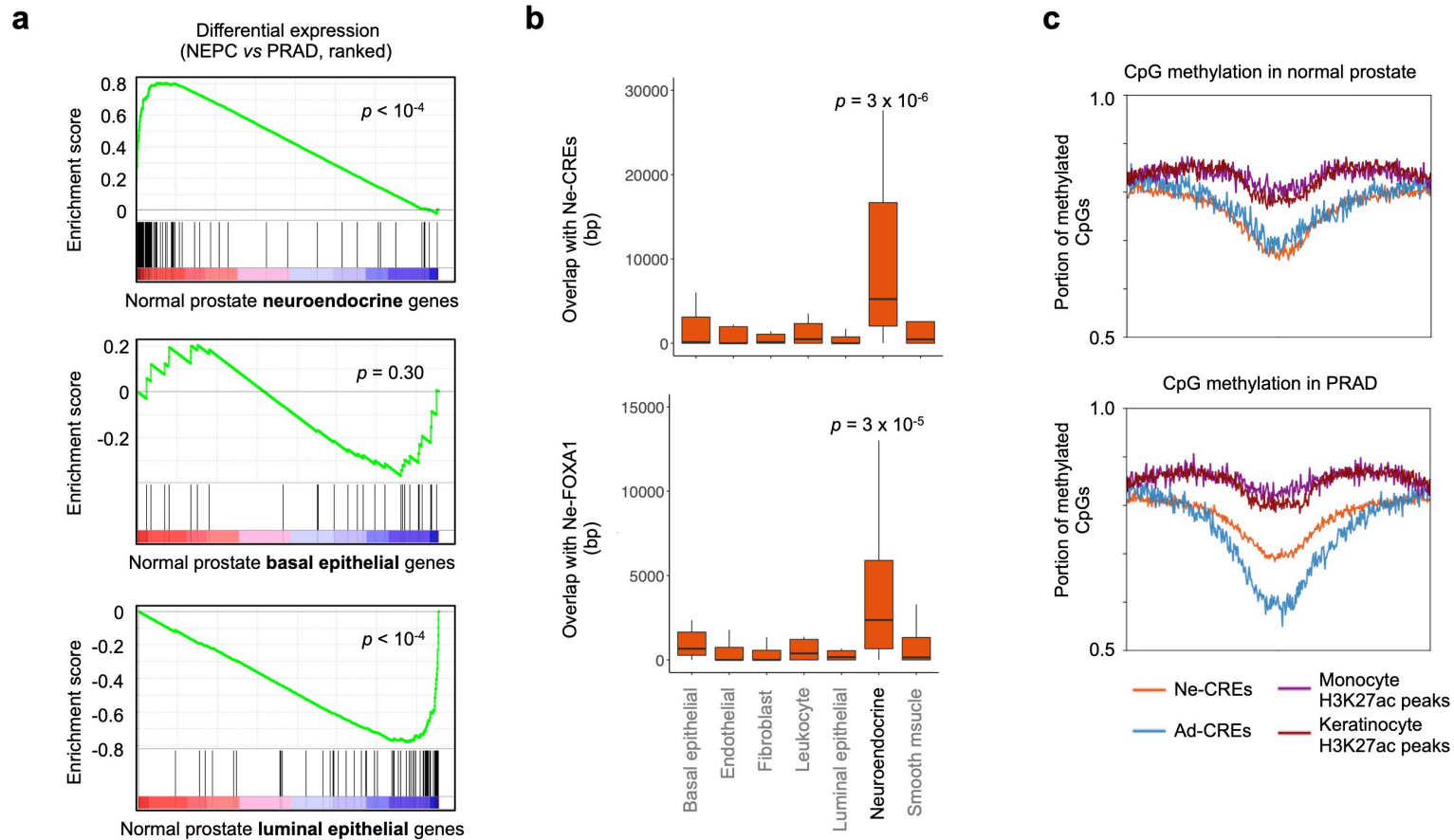
Figure 5. Gene expression of benign prostate cells compared to NEPC transcriptomes and epigenomes. a, Gene set enrichment analysis of genes specifically expressed in neuroendocrine, basal, and luminal cells from normal prostate[70]. Genes are ranked by differential expression in NEPC and PRAD LuCaP PDXs. **b**, Overlap of NEPC-enriched H3K27ac peaks (Ne-CREs; top) and FOXA1 binding sites (Ne-FOXA1; bottom) with a 200kb window centered on the transcriptional start site of the 20 most significantly differentially expressed genes in each indicated prostate cell type[70]. *p*-values correspond to Wilcoxon test of Ne-CRE/Ne-FOXA1 peak overlap near neuroendocrine cell genes versus all other indicated gene categories. **c**, fraction of CpG methylation detected by whole genome bisulfite sequencing in normal prostates tissue and PRAD at Ne-CREs and Ad-CREs. Methylation levels at H3K27ac peaks identified in epithelial keratinocytes or in peripheral blood monocytes are included for comparison. x-axis corresponds to peak center ±3kb.

5
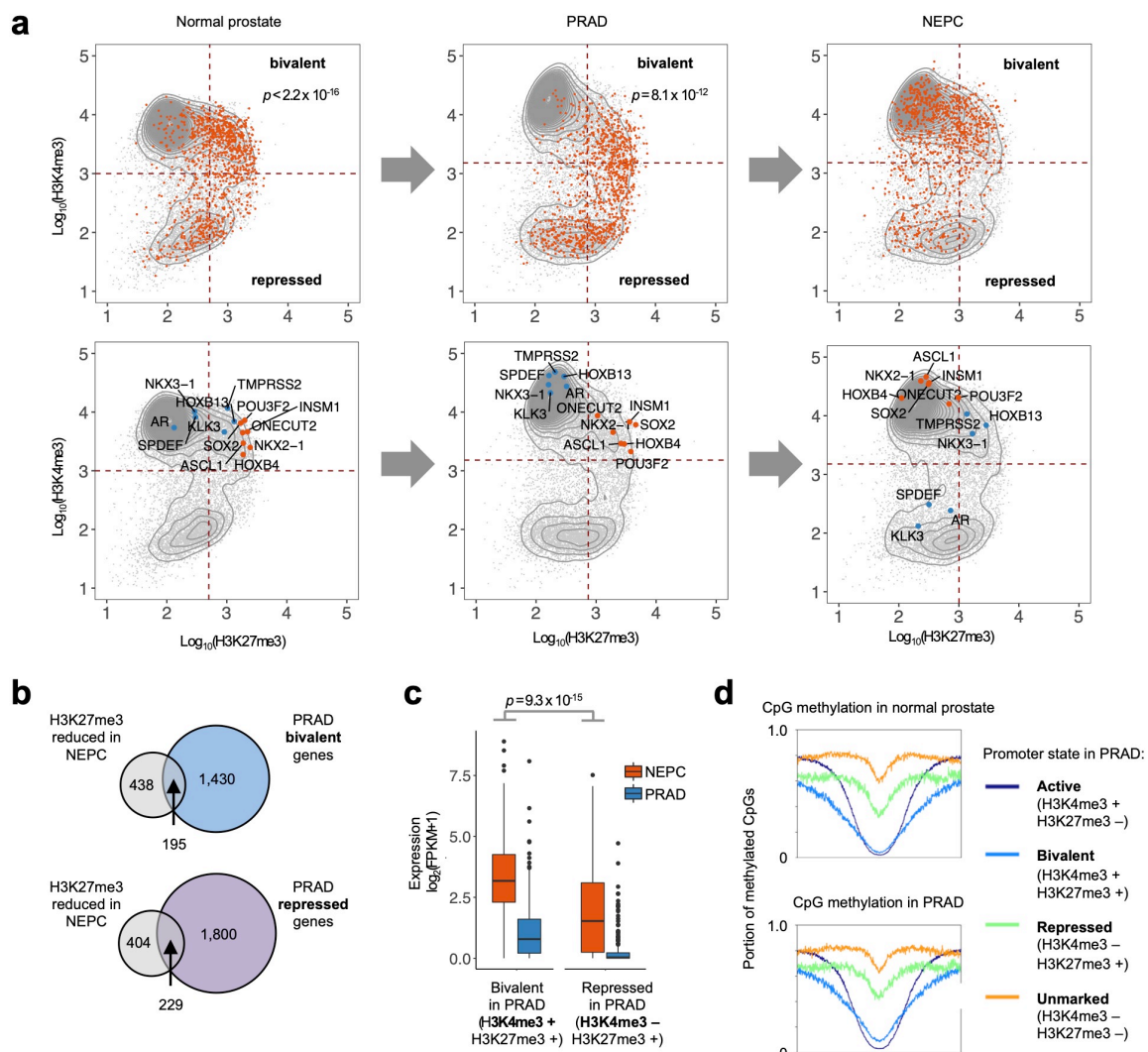
Figure 6. Encoding of neuroendocrine regulatory programs in the developmental history of prostate cancer. a, Average ChIP-seq tag density in normal prostate (n=3), PRAD (n=5) and NEPC (n=5) for H3K4me3 and H3K27me3 within 2kb of a gene transcriptional start site (TSS). Each dot represents a unique gene TSS. The top row highlights genes with upregulated expression in NEPC compared to PRAD (orange). p-values indicate Pearson's Chi-squared test comparing enrichment of upregulated genes within the "bivalent" quadrant compared to the bottom two quadrants. Selected genes are highlighted in the bottom row. **b**, Intersection of genes with bivalent (H3K27me3[+]/H3K4me3[+]) or repressed (H3K27me3[+]/H3K4me3[-]) promoter annotations in PRAD and genes with reduced promoter H3K27me3 in NEPC vs. PRAD ($\log_2$ fold-change < -1, FDR-adjusted p-value = 0.01). **c**, Transcript expression levels in NEPC of genes whose promoters lose H3K27me3 in NEPC compared to PRAD. Genes are grouped by bivalent or repressed promoter annotations in PRAD. p-value corresponds to Wilcoxon rank-sum test. **d**, Fraction of CpG methylation in normal prostate tissue and PRAD at TSS ± 3kb for genes in each indicated category.

6
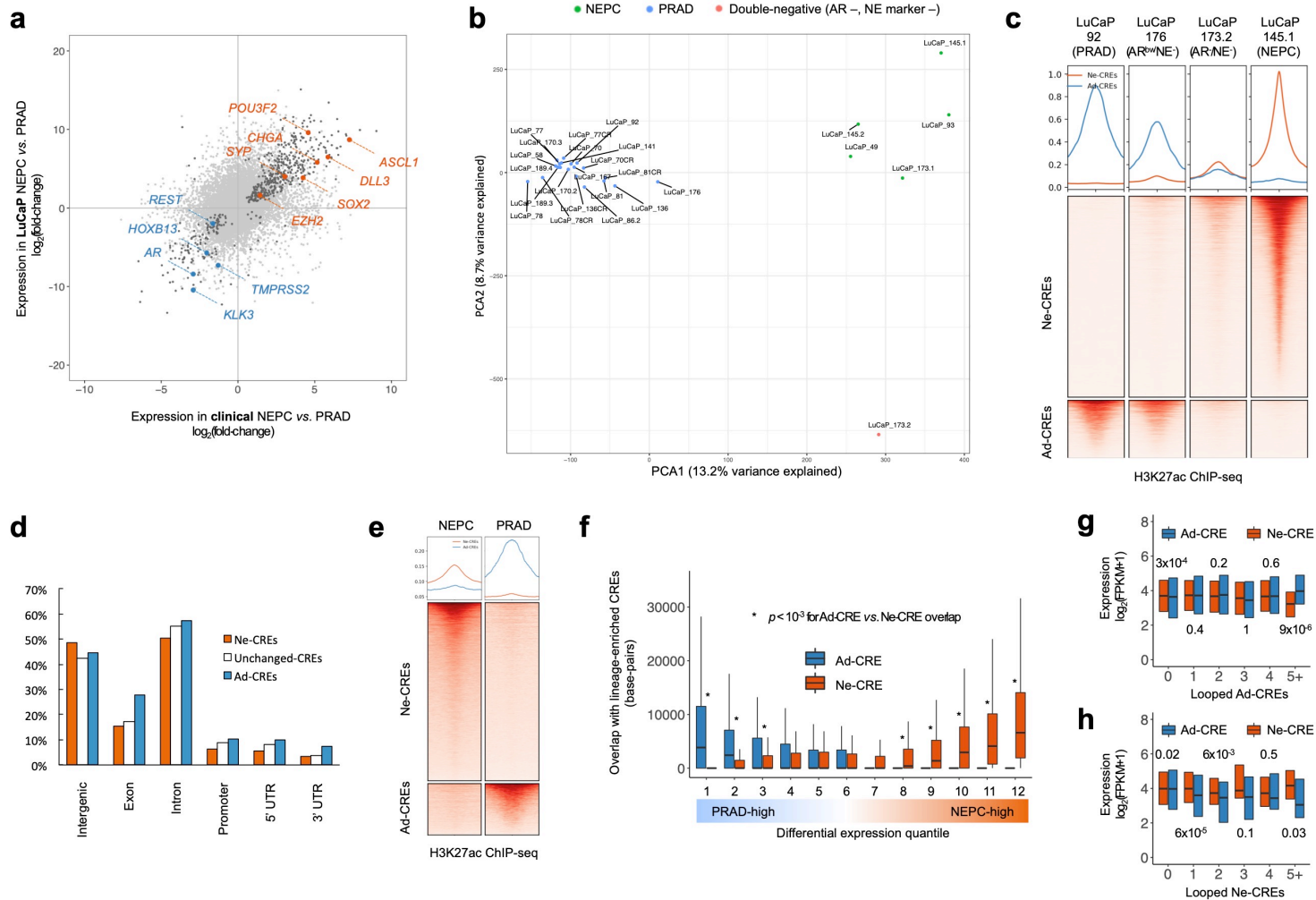
Supplementary Figure 1. Epigenomic divergence of NEPC and PRAD. a, Comparison of differential gene expression between PRAD and NEPC in LuCaP PDXs (5 of each lineage, with two replicates for each sample) and clinical prostate tumors[8]. Dark gray signifies genes with significant differential expression ($p<10^{-4}$) in both PDXs and clinical tumors. **b**, Principal component analysis of PRAD and NEPC PDXs based on H3K27ac profiles. "DN" indicates a "double-negative" PDX lacking AR or NE marker expression. **c**, Normalized H3K27ac tag density for AR^-/NE^- and AR^{low}/NE^- PDX at Ne-CREs and Ad-CREs, compared to representative PRAD and NEPC PDXs. Profile plots (top) indicate the average tag density at Ne-CREs (orange) and Ad-CREs (blue). **d,** Genomic annotations for lineage-specific and shared H3K27ac peaks. **e**, Normalized H3K27ac tag density at Ne-CREs and Ad-CREs in a clinical NEPC liver metastasis and a PRAD liver metastasis. Profile plots (top) indicate the average tag density at Ne-CREs (orange) and Ad-CREs (blue). **f**, Overlap of Ne-CREs and Ad-CREs with a 200kb window centered around the transcriptional start sites of differentially expressed genes. **g-h**, expression of genes with the indicated number of distinct looped Ad-CREs (g) or Ne-CREs (h) detected by H3K27ac HiChIP in LuCaP 173.1 (NEPC). All *p*-values were derived from Wilcoxon paired samples tests.
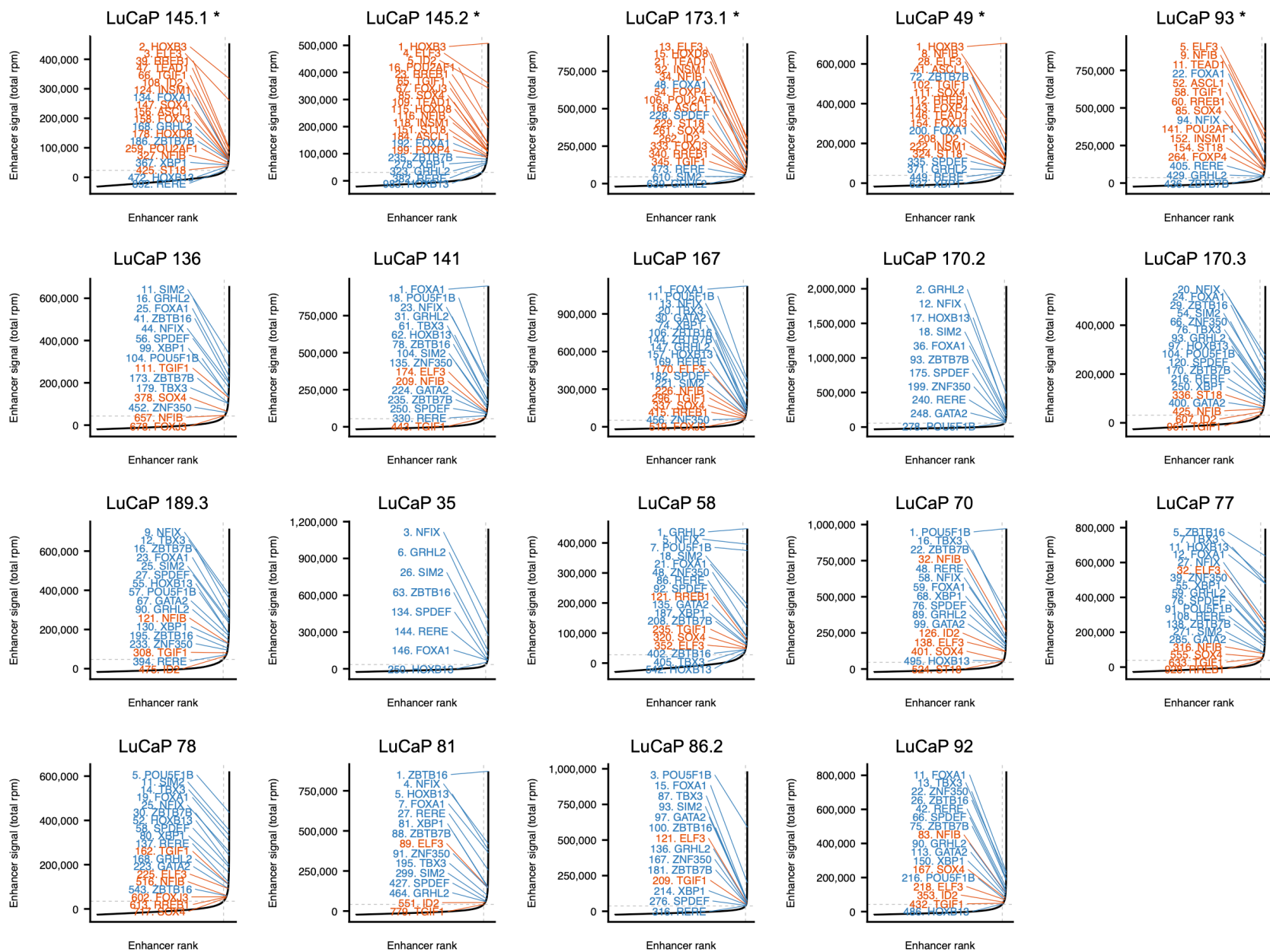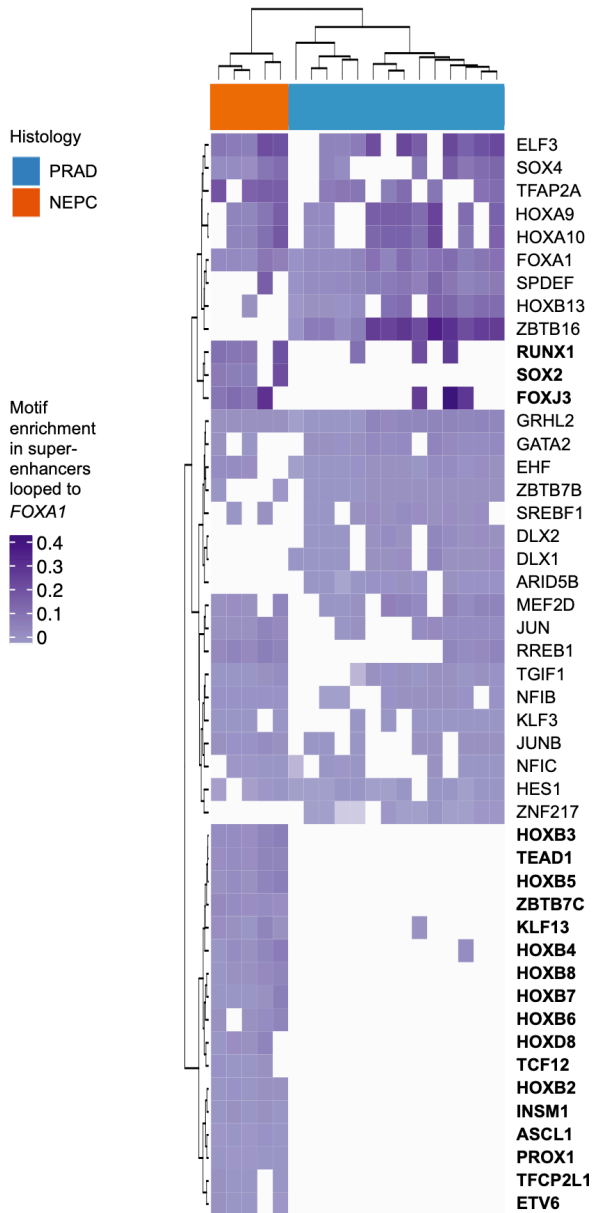
Supplementary Figure 2. Super-enhancers (SEs) encompassing transcription factor genes that are differentially H3K27 acetylated in NEPC *vs.* PRAD. SEs are ranked by H3K27ac signal. NEPC-enriched SEs are shown in orange; PRAD-enriched SEs are shown in blue (methods). Asterisk (*) indicates NEPC LuCaP PDXs.
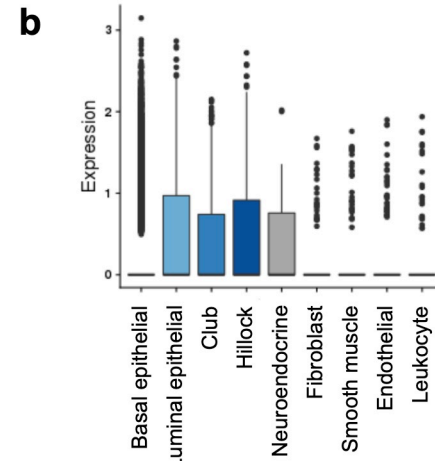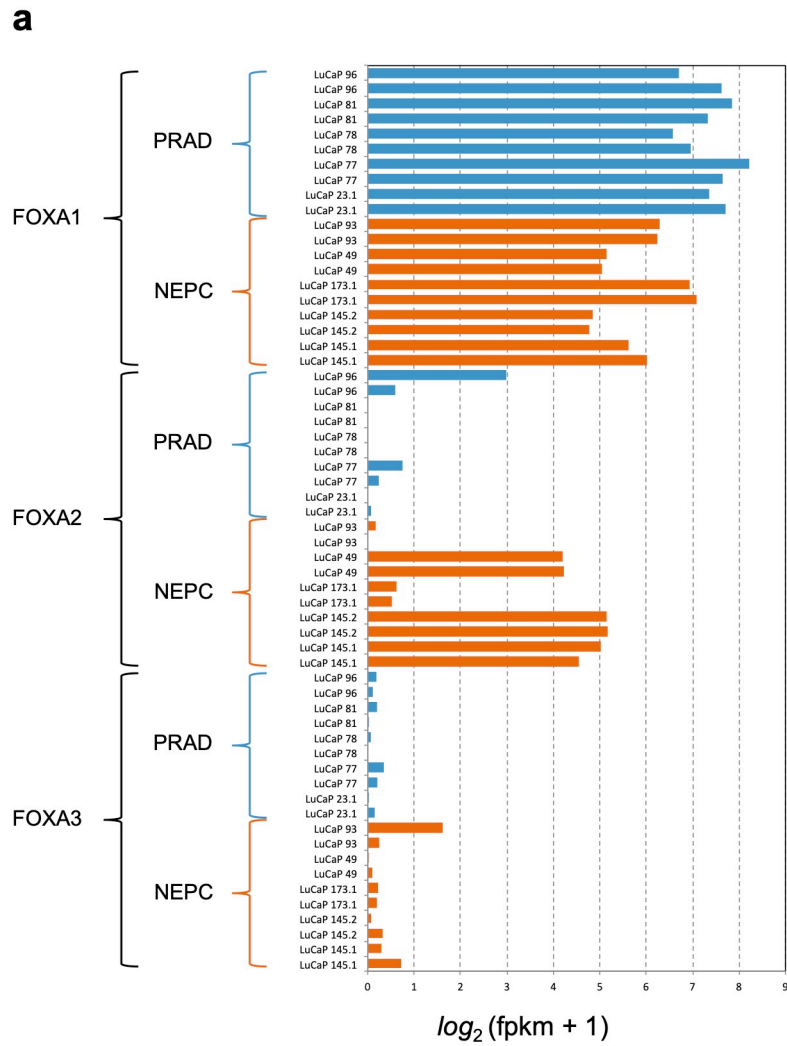
Supplementary Figure 3. Expression of FOXA1 in PRAD, NEPC, and benign prostatic tissue. **a**, Transcript expression of FOXA family members in 5 NEPC and 5 PRAD LuCaP PDXs (two replicates each) by RNA-seq. **b**, FOXA1 expression across benign prostate cell types in a published single-cell transcriptome sequencing dataset[70]. Boxes represent the interquartile range.

a

Motif	Enrichment *p*-value	Target	Background	TF
GGAGCTGTCCATGGTGCTGA	10^{-13}	12%	4%	REST

b
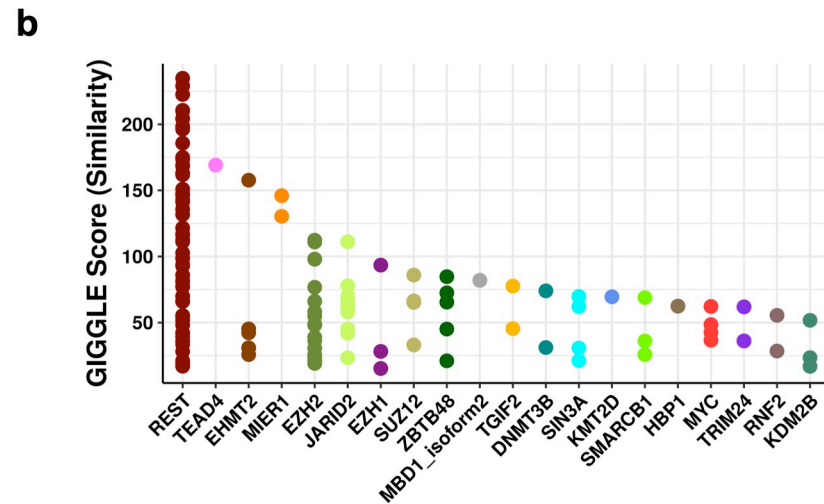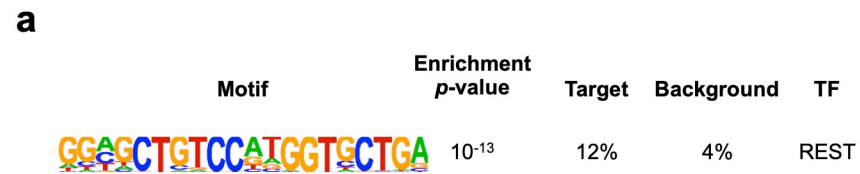
Supplementary Figure 4. Motif enrichment and TF binding of differentially H3K27 trimethylated promoters. a, Motif enrichment of promoters with diminished H3K27me3 in NEPC compared to PRAD. Only the indicated motif was significantly enriched. **b**, Cistromedb toolkit analysis of published ChIP-seq datasets (dbtoolkit.cistrome.org), ranked by their degree of overlap with the differentially H3K27 trimethylated promoters analyzed in **a**.

Supplementary Figure 5. Candidate TFs involved in regulation of the FOXA1 locus. Normalized abundance of TF binding motifs at superenhancers looped to the *FOXA1* locus, as assessed by H3K27ac Hi-ChIP in NEPC (LuCaP 173.1) and PRAD (LNCaP). TFs with motif enrichment primarily in NEPC are shown in bold.
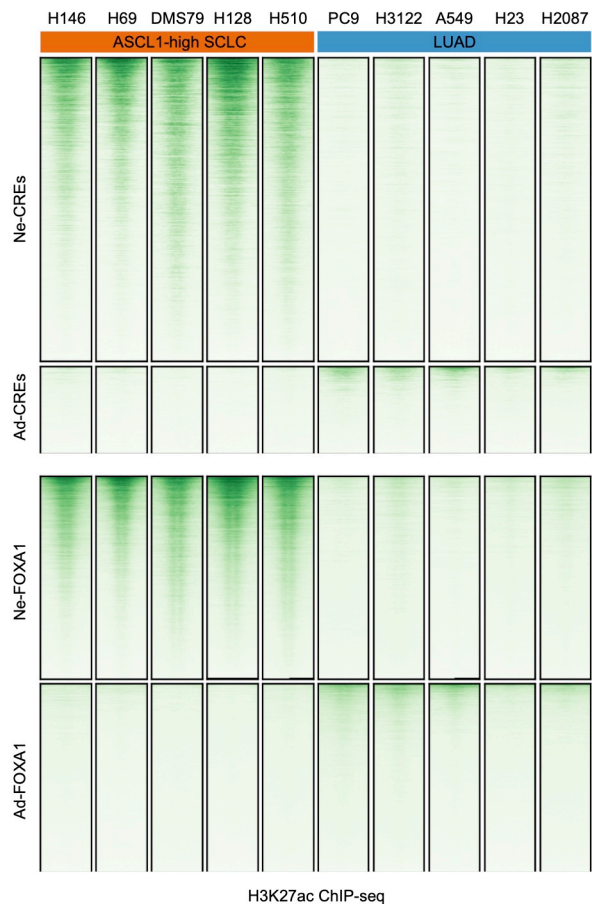
Supplementary Figure 6. Activation of neuroendocrine candidate regulatory elements in small cell lung cancer. H3K27ac ChIP-seq profiles of ASCL1-high small cell lung cancer (SCLC) cell lines[51] at Ne-CREs and Ad-CREs (top) and at NEPC-enriched and PRAD-enriched FOXA1 binding sites (bottom). Five lung adenocarcinoma (LUAD) cell lines are shown for comparison.